Germ-free C57BL/6 mice have increased bone mass and altered matrix properties but not decreased bone fracture resistance

Ghazal Vahidi[1], **Maya Moody**[2], **Hope D. Welhaven**[2], **Leah Davidson**[3], **Taraneh Rezaee**[4], **Ramina Behzad**[4], **Lamya Karim**[4], **Barbara A. Roggenbeck**[5], **Seth T. Walk**[5], **Stephan A. Martin**[6], **Ronald K. June**[1], **Chelsea M. Heveran**[1,#]

[1]Department of Mechanical & Industrial Engineering; Montana State University, Bozeman MT 59717

[2]Department of Chemistry & Biochemistry; Montana State University, Bozeman MT 59717

[3]Department of Chemical and Biological Engineering; University of Idaho, Moscow ID 83844

[4]Department of Bioengineering; University of Massachusetts, Dartmouth, MA 02747

[5]Department of Microbiology & Cell Biology, Montana State University; Bozeman MT 59717

[6]Translational Biomarkers Core Laboratory; Center for American Indian and Rural Health Equity; Montana State University, Bozeman MT 59717

Abstract

The gut microbiome impacts bone mass, which implies a disruption to bone homeostasis. However, it is not yet clear how the gut microbiome affects the regulation of bone mass and bone quality. We hypothesized that germ-free (GF) mice have increased bone mass and decreased bone toughness compared with conventionally-housed mice. We tested this hypothesis using adult (20 to 21-week-old) C57BL/6J GF and conventionally-raised female and male mice (n=6-10/group). Trabecular microarchitecture and cortical geometry were measured from microCT of the femur distal metaphysis and cortical midshaft. Whole-femur strength and estimated material properties were measured using three-point bending and notched fracture toughness. Bone matrix properties were measured for the cortical femur by quantitative backscattered electron imaging, nanoindentation, Raman spectroscopy, and for the humerus by fluorescent advanced glycation end-product assay (fAGEs). Shifts in cortical tissue metabolism were measured from the contralateral humerus. GF mice had reduced bone resorption, increased trabecular bone microarchitecture, increased tissue strength that was not explained by differences in bone size, increased tissue mineralization and fAGEs, and altered collagen structure that did not decrease

[#]Corresponding author: chelsea.heveran@montana.edu; 406-994-2010.

fracture toughness. We observed several sex differences in GF mice, most notably for bone tissue metabolism. Male GF mice had a greater signature of amino acid metabolism and female GF mice had a greater signature of lipid metabolism, exceeding the metabolic sex differences of the conventional mice. Together, these data demonstrate that the GF state in C57BL/6J mice alters bone mass and matrix properties but does not decrease bone fracture resistance.

Graphical Abstract:
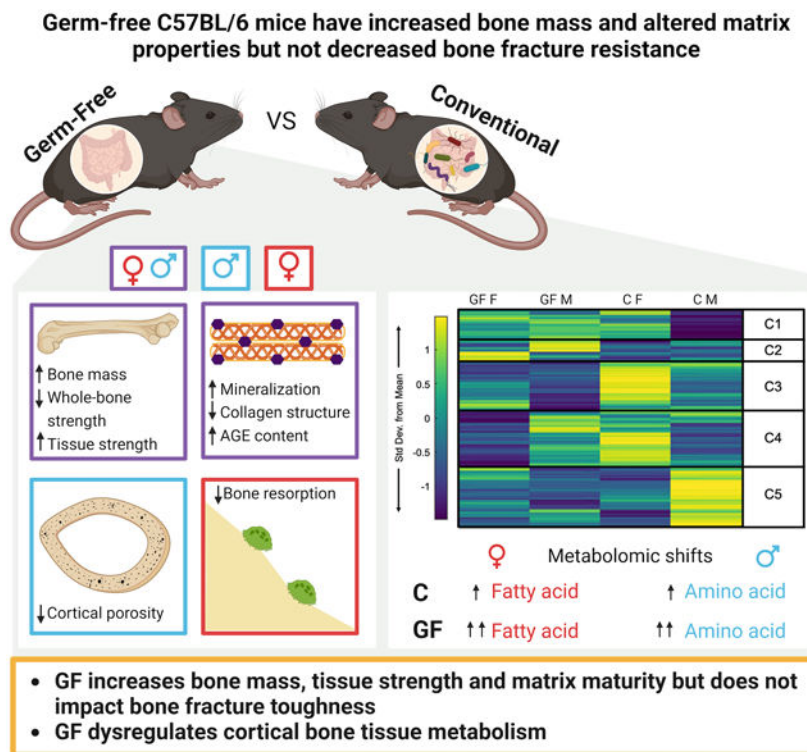
Germ-free (GF) mice have increased bone mass and tissue strength, but toughness is unchanged. GF increases both tissue mineralization and collagen maturity. The effect of GF shows several sex differences, starting at the level of bone tissue metabolism, where GF exacerbates sex differences that are seen in conventionally-raised (C) mice.

Keywords

gut microbiome; bone quality; bone strength; bone tissue metabolism; sex differences

1. Introduction

The mammalian gut microbiome is composed of trillions of microbial cells and is responsible for the production of a diverse set of molecules[1]. Evidence suggests that the composition of the gut microbiome can drive sex-dependent differences in host phenotype and disease[2-6]. Moreover, the composition of microbiome taxa itself is sexually dimorphic[2,7-11]. The repertoire of gut microbial antigens and metabolites can influence

bone mass through their impacts on nutrient transport, system regulation, and translocation of bacterial products into the systematic circulation and bones [9,12-17]. The gut microbiome may impact osteocytes directly by changing paracrine and endocrine signaling from trafficking immune cells[18]. However, whether the microbiome has sexually dimorphic effects on bone cells, bone tissue metabolism, and multiscale bone quality is still uncertain; therefore, important interactions between the gut and the skeleton may be masked.

Evaluation of hindlimbs from germ-free (GF) mice offers an important insight into the gut microbiome's role in normal bone homeostasis. Several studies using this approach reported that female GF C57BL/6 mice had increased bone mass, trabecular microstructure, and cortical geometry compared to conventionally raised female mice[10,19-22] (Table 1). Though the increased bone mass of GF mice implies the activities of osteoblasts and osteoclasts are dysregulated, the specific impacts of the gut microbiome on the abundance and activities of each of these cells are not clear. Because the GF immune system is not fully developed[9,19,23-25], osteoclast maturation would be expected to decrease. Sjorgen and coauthors reported a decrease in osteoclast abundance at the femur of 9-week-old GF mice[19], while Li *et al.* reported no change in osteoclast abundance at the femur of 12-week-old GF mice[20]. Similarly, Novince *et al* reported higher expression of osteoblast-related genes and proteins such as Runx2, Col12a, and osteocalcin in marrow cell cultures from the femur of 12-week-old GF mice[26], but Yan and coauthors reported lower expression of Runx2 in epiphyseal bone from 13-week-old GF mice[27] (Table 1). Therefore, whether and to what extent osteoblast and osteoclast abundance and activity in GF mice differ from those of conventional mice remains unclear.

Even less is known regarding osteocyte abundance and function in the GF state. For example, GF mice lack bacteria-driven vitamin K biosynthesis[9], which was shown to play an important role in osteoblast to osteocyte transition[28-32]. Therefore, it is possible that GF mice have fewer osteocytes. Currently, it is unknown whether osteocyte abundance, signaling, or perilacunar remodeling are disrupted in GF mice and whether these changes may also be dependent on sex. This particular knowledge gap is important because osteocytes are essential for indirectly and directly regulating bone mass and bone quality over the lifespan[33,34], and often have sexually dimorphic characteristics[35-37].

If the microbiome is important in bone cell physiology, it is plausible that at least some of the pathways involved depend on microbial metabolites either used directly by host cells for their own metabolism or indirectly as metabolic regulators, which is the case for other non-bone tissues[38]. Thus, there is a premise for interrogating whether bone tissue metabolism is also regulated by the microbiome. Studying the metabolism of bone tissue provides a snapshot of cellular-level bioenergetics, which aids the interpretation of differences in bone remodeling activity. We recently found that cortical bone metabolic pathways were sexually dimorphic in 20-week-old C57BL/6J mice[39]. These metabolic pathways were mostly attributed to osteocytes since cortical bone is mostly cellularized by osteocytes (>90%)[33,34]. However, it is likely that metabolites from bone marrow still persist in this tissue. We found that female mice had greater levels of lipid metabolism while male mice had higher levels of amino acid metabolism. Stronger bones, regardless of sex, had higher tryptophan and purine metabolism[39]. Assessing bone tissue metabolism for GF

and conventional mice of both sexes provides new insights into the connections between the microbiome, bone cell health, and bone quality.

Whether bone material properties in addition to bone mass and microarchitecture are altered in the GF model remains unknown. It is not yet understood if the GF state alters matrix properties, and whether these changes translate into differences in whole bone fracture resistance. In this study, we hypothesized that GF mice would have similar or greater bone strength, consistent with their expected increased bone mass, but impaired bone matrix properties and fracture toughness compared with conventionally-raised controls. We further hypothesized that the effects of the gut microbiome on the skeleton would interact with sex. Because the microbiome has a strong effect on cellular energy metabolism in other tissues[38], we also hypothesized that the alterations in bone quality in GF mice would extend to dysregulated bone tissue metabolism.

2. Materials and Methods

2.1 Animal model

All animal procedures were approved by Montana State University's Institutional Animal Care and Use Committee. Female and male GF C57BL/6J mice (female; n = 6, male; n = 7) were born and raised in standard cages inside hermetically sealed isolators with HEPA-filtered airflow and maintained on sterile (autoclaved) water and food (LabDiet® 5013, Land O'Lakes, developed specifically for autoclaving) ad libitum. Age- and sex-matched conventionally-raised C57BL/6J mice (female; n = 10, male; n = 10) were also used. Conventional mice were housed in cages of 3-5 mice and fed a standard chow diet ad libitum (LabDiet® 5053, Land O'Lakes. Supplemental Table 2 summarizes minor differences in the chow diets for GF and conventional animals). Male mice in each group were littermates since mixing males of different litters can lead to aggressive behavior and fighting. Female mice were combined from different litters to obtain comparable sample sizes. All GF and conventional mice were bred in house but ultimately sourced from Jackson Laboratory. Thus, conventionally raised and GF C57BL/6J mice were not necessarily from the same colonies.

GF status was confirmed using standard cultivation and molecular biology techniques[40]. Liquid 'bug' traps comprised of a mixture of drinking water and food were left open to the air inside of isolators and observed daily for signs of microbial growth (i.e., turbidity). Stool samples from mice were monitored prior to and throughout experiments for signs of growth on rich media under anaerobic and regular atmosphere conditions (Mueller–Hinton broth and agar plates). Bulk DNA was also extracted from stool samples (DNeasy PowerSoil Pro DNA isolation kit, Qiagen, Hilden, Germany) and used as a template for PCR targeting the bacterial 16S rRNA encoding gene (bacteria). GF status was confirmed through lack of growth and amplification by PCR. Alizarin label (30 mg/kg; SIGMA: A3882-1G) was administered sterilely via intraperitoneal injection, 3 days before euthanasia. The injection of alizarin labels in GF animals was conducted inside the GF isolator cages equipped with glove boxes with sterile syringes and needles. The alizarin label was double-sterile-filtered before injections. Animals were euthanized by isoflurane overdose and cervical dislocation at age 20-21 weeks.

2.2 Quantitative Reverse Transcription Polymerase Chain Reaction (qRT-PCR)

Marrow-flushed left tibiae were pulverized in liquid nitrogen and homogenized in Trizol (Life Technologies). Total RNA was isolated using a Qiagen RNeasy Mini Kit (Qiagen) according to the manufacturer's protocol. RNA was reverse transcribed into cDNA using a High-Capacity cDNA RT kit (Thermo Fisher Scientific). qRT-PCR gene expression analyses were conducted on an Applied Biosystems QuantStudio 5 platform using PR1MA qMax Gold SYBR Green Master Mix. Gene expressions for RankL (receptor activator of nuclear factor–kappa B Ligand), MMP2 (matrix metalloproteinases), MMP13 (Matrix metalloproteinase-13), MMP14 (Matrix metalloproteinase-14), OPG (osteoprotegerin), ACP (TRAP, Tartrate-resistant acid phosphatase), and CTSK (cathepsin K) were determined using the following primer sequences in Table 2. Target gene expression was normalized to 18S, and relative quantification was determined (Ct method). The RankL/OPG ratio was determined using Ct calculations.

2.3 Histology

Right tibiae were decalcified with EDTA disodium salt dihydrate, dehydrated in a graded ethanol series, embedded in paraffin, and serially sliced into 5-micron-thick horizontal cortical diaphysis sections. Full cortex cross-sections from each sample were stained with terminal deoxynucleotidyl transferase dUTP Nick End Labelling (TUNEL) and tartrate-resistant acid phosphatase (TRAP). Two cortical sections were analyzed per sample for both TUNEL and TRAP stains. Histological slides were imaged using a Nikon E-800 microscope (Nikon, Melville, NY) with 4x and 10x objectives. Image analysis was performed using Fiji ImageJ software (NIH). Total lacunae and empty lacunae were measured from 10x TUNEL-stained sections. The number of osteoclasts and pink-stained lacunae were obtained from TRAP-stained sections. Images taken with the 4x objective were used to determine the total cortical area (TUNEL) and endocortical perimeter (TRAP) (Supplemental Figure 1). Lacunar number density (numbers / mm^2), percentage empty lacunae (numbers of empty lacuna /numbers of all lacunae), osteoclast number density (number of TRAP-positive osteoclasts per endocortical perimeter), and TRP-positive lacunae number density (numbers/ mm^2) were calculated.

Bone marrow adiposity was measured as previously described[39], using hematoxylin and eosin (H&E) staining on longitudinally cut, 5 μm sections of the tibia. Sections were imaged, and bone marrow adiposity was quantified through manual segmentation. A custom MATLAB code was used to obtain mean adipocyte area (mm^2), marrow cavity area (mm^2), adipocyte count, and adipocyte number density (number of adipocytes per marrow cavity area).

2.4 Serum chemistry analysis

Serum collected via cardiac puncture at euthanasia was assessed for biomarkers of bone turnover (P1NP and CTX1). Serum P1NP was measured using a Mouse Procollagen 1 N-terminal Peptide (P1NP) ELISA kit (MBS703389, My BioSource) and CTX1 was measured using a Mouse Cross linked C terminal Telopeptide of type 1 collagen (CTX1) ELISA kit (MBS722404, My BioSource), according to the manufacturer's protocols.

2.5 Trabecular microarchitecture and cortical geometry

A high-resolution desktop micro-tomographic imaging system (μCT40, Scanco Medical AG) was used to assess the trabecular microstructure and cortical geometry of femurs. Left femurs were harvested and fresh frozen at −20°C in phosphate-buffered saline- (PBS) soaked gauze before microCT analysis. Scans were acquired using a 10 μm³ isotropic voxel size, 70 kVP, 114 μA, and 200 ms integration time. Scans were subjected to Gaussian filtration and segmentation with 0.8 value for Gauss sigma (i.e., width of the Gaussian function) and 1 value for support (i.e., size of the filter kernel or the area of the image that is used to compute the convolution) for both trabecular and cortical bone. Image acquisition and analysis protocols adhered to JBMR guidelines[41]. Trabecular microarchitecture was evaluated at the femoral distal metaphysis in a region beginning 200 μm superior to the top of the distal growth plate and extending 1500 μm proximally. The endocortical region of the bone was manually contoured to identify the trabeculae. Trabeculae were segmented from soft tissue with a 375 mgHA/cm³ threshold. Using the Scanco Trabecular Bone Morphometry Evaluation Script, the following architectural parameters were measured: bone volume fraction (BV/TV, %), trabecular bone mineral density (BMD, mgHA/cm³), connectivity density (Conn.D, 1/mm³), structural model index (SMI), trabecular bone surface to bone volume ratio (BS/BV, mm²/mm³), trabecular thickness (Tb.Th, mm), trabecular number (Tb.N, mm⁻¹), and trabecular separation (Tb.Sp, mm).

Cortical geometry was evaluated at the femoral mid-diaphysis in 50 transverse microCT slices (500 μm) in a region including the entire outermost edge of the cortex. Cortical bone was segmented with a fixed threshold of 700 mgHA/cm³. The following cortical parameters were measured; cortical bone area (Ct.Ar, mm²), medullary area (Ma.Ar, mm²), total cross-sectional area (bone + medullary area) (Tt.Ar, mm²), cortical tissue mineral density (Ct.TMD, mgHA/cm³), cortical thickness (Ct.Th, mm), minimum moment of inertia (I_{min}, mm⁴), polar moment of inertia (pMOI, mm⁴), the maximum radius perpendicular to the I_{min} direction (C_{min}, mm), and section modulus (mm³), which was calculated as the ratio of I_{min}/ C_{min}.

2.6 Whole-bone mechanical and tissue material properties

The left femurs were assessed for flexural material properties using three-point bending (1 kN load cell, Instron 5543, Norwood, MA). The test was performed on PBS-hydrated femurs to failure at a rate of 5 mm/min on a custom fixture with an 8 mm span. Femurs were positioned such that the posterior surface was in tension. Load-displacement data were used to calculate estimated whole bone mechanical properties and tissue material properties based on standard flexural equations for the mouse femur, using I_{min} and C_{min} values from microCT[42]. Whole bone mechanical properties include stiffness (N/mm), work to fracture (mJ), post-yield displacement, maximum load (N), and peak bending moment (N.mm, referred to as whole bone strength). Tissue material properties include ultimate stress (MPa, referred to as tissue strength; calculated as the peak bending moment divided by section modulus), yield stress (MPa), modulus (GPa), and toughness (MJ/m³, area under stress-strain curve until first failure). The yield point was identified using a secant method, where we defined the secant line as 90% of the measured stiffness from the linear-elastic

portion of the load-displacement curve. The intersection of the secant line and the load-displacement curve was the yield point.

Notched fracture toughness was evaluated for the right femurs, consistent with our description in Welhaven et al[39]. A custom device (Supplemental Figure 2) was used to notch the posterior surface of mid-shaft femurs to a target notch depth of 1/3 of the anterior-posterior width[43]. Bone hydration was maintained using PBS. Notched femurs were then tested to failure in three-point bending (1 kN load cell, Instron 5543) at a rate of 0.001 mm/s on a custom fixture with an 8 mm span[43]. Femurs were tested with the posterior surface in tension. Following the test, distal femurs were cleaned of marrow near the fracture surface and air-dried overnight. Fracture surfaces were imaged using field emission scanning electron microscopy (FESEM, Zeiss SUPRA 55VP) in variable pressure mode (VPSE, 20 Pa, 15 kV) (Supplemental Figure 3). A custom MATLAB code was used to assess cortical geometry and the initial notch half angle. Fracture toughness values (critical stress intensity factors, Kc_{max} and $Kc_{initiation}$) were calculated using the maximum load and yield load methods[43] (Equation 1). The notch geometry satisfied the thick-wall cylinder criteria proposed by Ritchie et al[43].

$$K_c = F_b \frac{P_{max\,or\,yield} S R_o}{\pi(R_o^4 - R_i^4)} \sqrt{\pi\left(\frac{R_0 + R_i}{2}\right)\theta_{init}} \tag{1}$$

Where F_b is the geometry constant for thick-walled cylinders, P_{max} or P_{yield} are the max load or yield load, R_0 and R_i are mean outer and inner radii, S is the span of loading (8 mm), and θ_{init} is the initial notch half angle.

2.7 Quantitative histomorphometry

PMMA-embedded left distal femurs were used for quantitative histomorphometry. Following whole-bone mechanical testing, the left femurs were histologically dehydrated in a graded ethanol series (EtOH 70-100%) and embedded in poly(methyl) methacrylate (PMMA). The cortical cross-sections of the distal femurs were polished for further analyses. The polishing procedure included 600 and 1200 grits of wet silicon carbide papers (Buehler, Lake Bluff, IL) followed by fine polishing with Rayon fine cloths (South Bay Technologies, San Clemente, CA) and a series of alumina suspensions (9, 5, 3, 1, 0.5, 0.3, and 0.05 μm). Between each step, samples were sonicated with tap water to remove the remaining alumina particles. An upright confocal laser scanning microscope (Leica SP3, Heildelberg GmbH, Mannheim, Germany) was used to visualize the alizarin-fluorochrome-labeled periosteal and endocortical perimeters of the full cortex cross-section in the embedded cortical femur at the midshaft. Imaging was performed with the following parameters: 5x objective, laser wavelength excitation 633 nm (emission length 580-645 nm), 600 Hz speed with a 1024 × 1024 resolution, and pinhole set at 1 Airy unit. The gain and offset were set to the best label visibility and minimum noise per sample. ImageJ was used for image processing. Confocal images were converted to a maximum contrast to visualize reliably labeled bones and achieve consistent thresholding. Then, the perimeter of alizarin labeled (L.Pm) bone for endocortical and periosteal surfaces was measured. Total endocortical and periosteal bone perimeters (Tt.Pm) were also calculated. Percentage mineralizing surface (MS/BS=(L.Pm/

Tt.Pm)×100) was reported for endocortical and (Ec.MS/BS) periosteal surfaces (Ps.MS/BS) for each group. Animals that did not receive labels were excluded from this analysis.

2.8 Microscale assessment of cortical femur tissue modulus

PMMA-embedded (i.e., dehydrated, PMMA-embedded, and polished) left femurs were used for assessment of bone tissue modulus. Nanoindentation (KLA Tencor iMicro, Milpitas, CA) was performed on the posterior quadrant of each femur using a Berkovich tip. The target load of 5 mN was applied with a load function of 30 s load, 60 s hold to dissipate viscoelastic energy before unloading[44], and 30 s unload. Each nanoindentation map included three columns of indents spanning the whole cortical thickness (15 μm spacing in x and y; Figure 1A). The mean and standard deviation of the nanoindentation modulus map were calculated for each femur using the Oliver-Phar approach[45]. The 95th-45th percentile of the unloading curve was fit with a 2nd-order polynomial. A tangent line to the beginning of this section was used to calculate the stiffness (S, the slope of the unloading curve evaluated at the maximum load, $\frac{dP}{dh}$, Figure 1B). The tip contact area (A_c) was calculated as a function of the contact depth. The tip area was calibrated using fused silica (KLA Tencor, Milpitas, CA). The reduced modulus, E_r, was calculated from S and A_c (Equation 2).

$$E_r = \frac{S}{2}\sqrt{\frac{\pi}{A_c}} \tag{2}$$

$$\frac{1}{E_r} = \frac{1 - v_s2}{E_s} + \frac{1 - v_t2}{E_t} \tag{3}$$

Nanoindentation modulus (E_i) was then calculated from Equations 3-4, where the subscript s refers to the sample under study. E_t and v_t are the known tip modulus (1140 GPa) and Poisson's ratio (0.07), respectively. Since the sample's Poisson's ratio (v_s) is unknown, we report the indentation modulus E_i, eliminating errors from an assumption for v_s (Equation 4).

$$E_i = \frac{E_s}{1 - v_s2} \tag{4}$$

2.9 Microscale assessment of bone mineralization and porosity

Following nanoindentation, samples were coated with a thin layer of carbon for quantitative backscattered scanning electron imaging (qBEI, Zeiss Supra 55VP field emission SEM, 20 kV, 60 μm aperture size, 100x magnification, and 9.1 mm working distance)[46-48]. A custom steel sample holder equipped with springs that pushes polished embedded bone samples against a flat steel cover plate was used to ensure both flat sample surfaces and consistent working distances (Supplemental Figure 4). Images of the cortical cross-sections were collected at 100x magnification (Figure 1C). Polished carbon and aluminum reference standards (Electron Microscopy Services) were mounted on the sample holder and imaged with bone samples with each imaging session. Images were processed by setting the mean

grey levels of the aluminum and carbon calibration standards to 255 and 0, respectively[49]. A custom MATLAB code was used to convert the BSE images to corresponding calcium concentration, where each step in the greyscale corresponds with an increase of 0.1385 weight % calcium. Histograms of bone mineral density distribution with a bin size of 1 grey level were generated for each calibrated image. From histograms, Ca_{Peak}, the most frequent calcium concentration of the cortical surface (histogram peak), and Ca_{Width}, heterogeneity of the Ca concentration within each sample (full-width at half-maximum of the histogram[50]) were calculated (Figure 1D). To assess variation between imaging sessions, we imaged one control bone sample at each of the twelve imaging sessions and calculated the coefficient of variation (standard deviation/mean) in the Ca_{Peak} measurement of this control bone. We observed 0.85% variability in Ca_{Peak} for this control bone between imaging sessions (Figure 1E).

Cortical porosity was assessed for each bone from a 400x image of the posterior cortical surface taken in secondary electron mode (SE2, Zeiss Supra 55VP, 20 kV, 30 μm aperture size, 9.1 mm working distance). A custom MATLAB code was used to calculate the total porosity (%) and pore number density (number of pores per area of interest, $1/mm^2$). Pores greater than 150 pixels^2 were considered vasculature and pores smaller than this number were considered lacunae.

2.10 Microscale assessment of bone matrix properties

Tissue composition and collagen properties were assessed using Raman spectroscopy (laser-tweezer confocal Raman microscope, Modified LabRAM HR Evolution Raman Spectrometer, HORIBA, Japan) on hydrated right humeri. Humeri were thawed, cleaned, and flushed of marrow. For each sample, 5 spectra were collected from the posterior side, located 50 μm apart (Figure 2). The location of the deltoid tuberosity was used as a marker for the first spectrum point (black point in Figure 2) and other points were spaced approximately 50 micrometers apart. Raman parameters were: 10x dry objective lens (NA=0.25), 785 nm edge laser at 100% power, 300-1900 nm Raman spectra range, 30 accumulations for 4 second acquisition time. The spectrometer (800 mm focal length) was equipped with a 600 nm grating (300 lines per mm grating) which with a 785 nm laser provided a 1.5 cm^{-1} spectral dispersion. Bones were kept hydrated during the test, using a sponge bed and tap water. Background fluorescence was removed from all spectra using a 12th-order polynomial fit in the LabSpec 6 software (Horiba Jobin Yvon, Edison). Spectra were then analyzed using a custom MATLAB code. We measured mineral to matrix ratio (ν_2PO_4 (385-495 cm^{-1})/ amide III (1215-1295 cm^{-1})), carbonate to phosphate ratio (ν_1CO_3 (1053-1090 cm^{-1})/ ν_1PO_4 (920-990 cm^{-1}), indicative of the extent of carbonate substitution into the mineral crystal lattice), and crystallinity (full-width at half maximum of the ν_1PO_4 peak, FWHM $[\nu_1PO_4]^{-1}$). For these measurements, area ratios were calculated.

The signal-to-noise ratio for amide I sub-bands was further minimized for each Raman spectrum, using a Savitzky-Golay (S-G) filter. We identified the locations of amide I sub-bands based on the second derivative method and from these locations' measured intensities[51-53]. Amide I sub-band ratios were calculated, including $_{1670}/I_{1610}$ and I_{1670}/I_{1640}. The following ranges were used to locate the amide I sub-band peaks: 1610 cm^{-1}

(1600-1620 cm^{-1}), 1640 cm^{-1} (1633-1645 cm^{-1}), and 1670 cm^{-1} (1660-1680 cm^{-1}). For all Raman measurements, spectra were processed individually, and then peak intensity ratios were averaged over the 5 spectra per bone.

2.11 Assessment of fluorescent advanced glycation end-products (AGEs)

Right humeri were cleaned of all soft tissue, flushed to remove bone marrow, and proximal and distal ends removed such that only diaphyseal cortical bone was used in the measurement of total fluorescent AGEs (fAGEs). Quantification and normalization of fAGEs to collagen content followed previously published protocols[54-58]. Briefly, the specimens were defatted by three 15-min washes in 200 μL 100% isopropyl ether while being agitated. Specimens were then lyophilized for 8 hours using a FreeZone 2.5 Liter freeze-dry system (Labconco, Kansas City, MO) and hydrolyzed based on dry mass in 6 N HCl (10 μL/mg bone) for 20 hours at 110°C. Hydrosylates were diluted 100X and then centrifuged at 13,000 RPM at 4°C to remove any debris. Hydrolysates were stored at −80° C in complete darkness until use. Fluorescence was measured at 360/460 nm excitation/ emission for the diluted hydrolysates and quinine standards (stock: 10,000 ng/mL quinine sulfate per 0.1 N H2SO4) using a Synergy HTX Multi-Mode Reader (BioTek, Winooski, VT). For quantification of hydroxyproline, first, a chloramine-T solution was added to the diluted hydrolysates and hydroxyproline standards (stock: 2,000 μg/mL L-hydroxyproline per 0.001 N HCl) and incubated at room temperature for 20 min to oxidize hydroxyproline. To quench residual chloramine-T, perchloric acid (3.15 M) was added and incubated at room temperature for 5 min. Lastly, a p-dimethylaminobenzaldehyde solution was added and incubated at 60° C for 20 min. All of the samples and hydroxyproline standards were cooled to room temperature while in complete darkness. Once cooled, absorbance was measured at 570 nm using the same plate reader listed above for the processed hydrosylates and hydroxyproline standards. The measured hydroxyproline quantity for each specimen was used to calculate collagen content[59] and total fluorescent AGEs were reported as ng quinine/mg collagen.

2.12 Evaluation of cortical bone metabolism

To investigate the metabolism of cortical bone, humeri-derived metabolites were subjected to liquid chromatography-mass spectrometry (LC-MS) and global metabolomic profiling was employed for the cortical bone of the humerus as previously reported[39]. Humeri ends were trimmed and flushed of marrow with PBS to isolate cortical bone and then stored fresh-frozen at −20°C in PBS-soaked gauze. Next, humeri were placed in liquid nitrogen for 2 hours and pulverized to optimize metabolite extraction. Pulverized bone was then precipitated with methanol:acetone, vortexed for one minute, and incubated at −20°C for four minutes. This process was repeated five times. Samples were then incubated overnight at −20°C to promote precipitation. The following day, the samples were centrifuged and supernatant was dried down via vacuum concentration. Once dry, samples were suspended in acetonitrile:water.

Samples were analyzed using LC-MS (Agilent 6538 Q-TOF mass spectrometer) in positive mode (resolution: ~20 ppm, adducts: H+, Na+) using a Cogent Diamond Hydride HILIC chromatography column, as previously described[39,60,61]. Agilent Masshunter Qualitative

software, XCMS, MetaboAnalyst, and MATLAB were used for data analysis. Raw data were log-transformed and auto-scaled (mean-centered divided by standard deviation per variable) prior to analysis. Statistical analyses included hierarchical cluster analysis (HCA), principal component analysis (PCA), partial least squares-discriminant analysis (PLS-DA), volcano plot analysis, t-test, and fold change. MATLAB was utilized to examine differences in metabolite intensity across experimental groups. MetaboAnalyst's Functional Analysis tool was used to identify biologically relevant pathways that are dysregulated between experimental groups (GF, sex, and GF-sex interactions).

2.13 Statistical analysis

We tested whether bone characterization outcomes depended on microbiome status (GF vs. conventional), sex (female vs. male), or their interaction (Minitab, v.20). We used two-way ANCOVA models with body mass as a covariate to test whether body mass differences between the groups could explain the impacts of GF, sex, or interaction on bone properties. When the covariate effect was insignificant, the model was run again without it (i.e., ANOVA). Dependent variables were transformed, if necessary, such that all models satisfied assumptions of residual normality and homoscedasticity. Significance for GF main effect, sex main effect, or GF and sex interaction was set *a priori* to $p < 0.05$. Significant interactions between GF and sex were followed up with post-hoc tests, and GF vs. conventional was compared within each sex (i.e., two comparisons, critical α: 0.05/2 = 0.025; Bonferroni correction to maintain family-wise type I error). When there was a significant interaction, the p-values of post-hoc comparisons were reported. Nanoindentation and Raman measurements were averaged per mouse such that one mean and one standard deviation for each measure per mouse were input into ANOVA models. Percent differences for significant main effects were calculated by pooling across both levels of the other factor (e.g., pooling males and females to calculate the percent difference between GF and conventional). In the case of a significant interaction between GF and sex, percent differences were calculated between GF and conventional mice of each sex. We tested the power of our analyses using G*Power Version 3.1.9.4. Power analyses (t-test, differences between two independent means) were conducted for the effect of GF vs. conventional within each sex. The Cohen's d effect size was measured using the mean and standard deviation values for each group. Then, the required sample sizes to achieve power of 0.8 were calculated using the same effect size, $\alpha = 0.05$, and an allocation ratio of 1.

3. Results

3.1 The effect of the gut microbiome on body weight depends on sex

GF and sex had an interactive effect ($p = 0.001$) on terminal body weights such that GF females were heavier than conventional females (+23.4%, 18.6%, $p < 0.001$), but weights were not different between GF and conventional males. Femur length was similar across groups (Table 3).

3.2 The gut microbiome affects gene expression related to bone turnover

OPG expression from the marrow-flushed tibia was lower in GF mice compared to conventional mice (−51.6%, $p = 0.032$) (Figure 3). RankL expression was similar among

groups. The RankL/OPG ratio was higher in GF mice compared to conventional mice (+127.6%, p = 0.033). We also assessed the expression of several genes involved in osteocyte perilacunar remodeling. MMP2 expression decreased with GF (−39.7%, p = 0.044) and the interaction between GF and sex on MMP2 expression was not significant (p = 0.07). MMP13 expression did not differ with GF or sex. MMP14 was expressed more in females compared to males (+64.0%, p = 0.030) but was unchanged with GF. CTSK expression was lower in females than males (+112.8%, p = 0.031) but not changed with GF. ACP5 did not differ with sex or GF.

3.3 The effects of the gut microbiome on local and global bone turnover depend on sex

Sex and GF had an interactive effect on osteoclast number density, such that only GF females had reduced osteoclasts per endocortical perimeter (i.e., osteoclast number density) compared to conventional mice (−75.5%; p = 0.022, Figure 4A). Osteocyte perilacunar bone resorption, as estimated from TRAP-positive lacunae, was decreased in females and GF overall (−67%, p = 0.043; −155%, p = 0.021, respectively, Figure 4B). In contrast, lacunar number density and percent empty lacunae were not influenced by microbiome status or sex (Figure 4C-D).

Serum P1NP was higher in GF mice compared to conventional mice (+19.9%, p = 0.03) and in males compared to females (+20.7%, p = 0.008) (Figure 5A). Serum CTX1 had a significant interaction between GF and sex (p = 0.036) such that CTX1 level was similar among GF and conventional males but lower and more homogenous in GF females compared with conventional females (−29.7%, p =0.019) (Figure 5B). The CTX1/P1NP ratio was lower with GF in both sexes (−26.3%, p = 0.001) and was also higher in females compared to males (+57.6%, p < 0.001) (Figure 5C).

Both sex and GF influenced alizarin mineralizing surface (MS/BS) at the midshaft femur (Table 4). For the periosteal surface, GF mice had higher MS/BS values compared to the conventional mice (+50.6%, p = 0.005). Females had higher MS/BS values compared to males for both periosteal and endocortical surfaces (+29.2%, p = 0.04 and +36.1%, p = 0.046, respectively).

3.4 The gut microbiome does not affect marrow adiposity

Bone marrow adiposity analysis revealed differences in adiposity between mice that differed by sex and GF (Supplemental Table 1). Mean marrow cavity area was lower with GF compared to conventional mice (−21%, p = 0.001) and for females compared to males (−20%, p = 0.001). Adipocyte counts (−25%, p = 0.02) were decreased with GF. They were also higher in females compared to males (+359%, p < 0.001). Consequently, adipocyte number density (number of adipocytes per marrow area) was similar between GF and conventional mice and higher in females compared to males (+452%, p < 0.001). Adipocyte size did not differ with GF or sex.

3.5 The effects of the gut microbiome on trabecular microstructure and cortical geometry depend on sex

GF increased trabecular bone microstructure, but the effect was more pronounced for males (Table 5). BV/TV was higher in GF mice compared to conventional mice (+17.4%, p = 0.05) and was lower in females compared to males (−63.1%, p < 0.001). Similarly, Tb.BMD increased with GF (+9.6%, p = 0.05) and was lower in females compared to males (−41.0%, p < 0.001). The structural modulus index showed more rod-like trabeculae for females (SMI~3) and more plate-like in males (SMI~1.5), but GF did not affect this measure. GF and sex had an interactive effect on connectivity density, such that Conn.D greatly increased for GF males (+79.1%, p < 0.001) but remained unchanged for GF females compared to their respective conventional mice. GF and sex also had an interactive effect on Tb.Th, Tb.N and Tb.Sp, such that GF only affected these properties in males and not females. Tb.Th and Tb.Sp were lower in GF males compared to conventional males (−13.0%, p = 0.001 and −22.9%, p < 0.001, respectively). Tb.N was higher in GF males compared to conventional males (+25.6%, p < 0.001).

The effect of GF on bone cortical geometry was different between males and females (Table 5). GF and sex had an interactive effect on section modulus and I_{min} such that GF males had lower I_{min} and section modulus (−27.1%, p <0.001; −34.8%, p <0.001) and GF females had slightly higher I_{min} and section modulus (+1.5%, p =0.021; +9.0%, p = 0.04) compared to their respective conventional groups (Figure 7A-B). GF and sex had an interactive effect on pMOI (p = 0.004) such that GF males had 36% lower pMOI compared to conventional males, whereas GF females have only 4% lower pMOI values compared to conventional females. Ct.Ar was decreased with GF in both males and females (−9.5%, p <0.001). Cortical thickness increased with the female sex (+10.7%, p < 0.001) but was unchanged with GF. Ct.TMD was slightly lower with GF (−1.2%, p = 0.003) and female sex (+3.8%, p < 0.001). The effect of GF on cortical geometry remained significant even after accounting for the linear relationship between geometry and body mass seen in several measurements (Supplemental Table 1, Supplemental Figure 5A).

Cortical bone porosity, estimated from SEM, showed an interactive effect of GF and sex (p= 0.023) such that total porosity was decreased for GF males compared to conventional males (−19.6%, p =0.019) but was unchanged for GF females versus conventional females (Figure 6A). Pore number density was also not different among groups (Figure 6B). Lacunar porosity and vascular porosity were not different among groups (Figure 6C-D).

3.6 The absence of the gut microbiome decreases whole bone strength but increases tissue strength and modulus

GF decreased whole bone strength (i.e., peak bending moment) and maximum load (−3%, p=0.042; −4%, p=0.042, respectively). In males, these differences were largely explained by variance in geometry (Figure 7A). In females, differences in whole bone strength were not explained by variance in geometry between GF and conventional groups. Tissue strength (i.e., ultimate stress) was higher in GF mice of both sexes (+13.0%, p < 0.001) compared to conventional mice and was also higher in females compared to males (+15.5%, p < 0.001) (Figure 7C). Similarly, modulus depended on both GF and sex. Specifically, GF mice had

higher tissue modulus (+11.7%, p = 0.006) compared with conventional mice (Figure 7D). Females also had higher tissue modulus (+19.2%, p < 0.001) than males. While whole bone properties depended on body mass (i.e., larger mice have greater whole bone strength), the estimated material properties did not (Figure 7C-D, Supplemental Figure 5). Complete results from three-point bending are reported in Supplemental Table 1.

The critical stress intensity factor calculated at the maximum load (Kc_{max}) and at crack growth initiation ($Kc_{initiation}$) from notched fracture testing did not differ with GF or sex. Notably, the effect of GF on Kc_{max} was likely underpowered in females. It is possible that the addition of a few more bones (n=11 per group of females) could reveal an increase in Kc_{max} for GF females versus conventional females (Figure 7E, Supplemental Table 1).

3.7 The absence of the gut microbiome increases tissue mineralization and impacts collagen structure and AGE accumulation

The mineral-to-matrix ratio ($\nu_2 PO_4$ / Amide III) from Raman spectroscopy was higher in GF mice compared to conventional mice for both sexes (+6%, p = 0.024) (Figure 8A). Mineral maturity, as indicated by carbonate to phosphate ratio (carbonate substitution, $\nu_1 CO_3$ / $\nu_1 PO_4$) (Figure 8B), and crystallinity (Supplemental Table 1) were not affected by GF or sex. There were no main effects of sex or sex-GF interactions on Raman measurements of bone composition. Ca_{Peak} values from qBEI were slightly higher (+3.0%, p = 0.018) with GF but were not affected by sex (Figure 9A). Ca_{Width} values were similar among all groups (Supplemental Table 1). GF increased the mean nanoindentation modulus only for males (+8.4%, p = 0.023, Figure 9B). The standard deviation of E_i was unaffected by GF or sex (Supplemental Table 1).

GF also affected several properties related to collagen. From Raman spectroscopy, GF was observed to impact amide I subpeak intensity ratios. Disruption in the helical status of the collagen can indicate a transition from an ordered triple helical structure to less-ordered forms of structures in collagen[62,63]. The amide I sub-band ratio I_{1670}/I_{1640} was slightly higher with GF (+3.5%, p = 0.050) while I_{1670}/I_{1610} was more increased with GF (+8.3%, p = 0.011) (Figure 8C-D). There was no effect of sex or interaction between sex and GF on these or other Raman measurements. Cortical fAGEs content in the humerus was higher (+103%, p = 0.001) in GF bones compared to conventional specimens (Supplemental Table 1). Sex did not affect fAGEs, and there was no interaction between GF and sex on fAGE content.

3.8 Alterations in whole bone quality with microbiome status are multifactorial

The correlations between whole bone mechanical properties (whole bone strength) and estimated tissue material properties (tissue strength, modulus, and fracture toughness) with tissue mineralization (Ca_{Peak}), collagen structure, cortical porosity, and bone turnover parameters including Ps. MS/BS (alizarin mineralizing surface) and osteoclast number density were tested using Spearman's correlation (95% CI). We found that Ca_{Peak} from qBEI was positively correlated with tissue strength (i.e., ultimate stress, Spearman's ρ = 0.49, p = 0.006) and modulus (ρ = 0.47, p = 0.009). However, Ca_{Peak} was not correlated with whole bone strength (i.e., peak bending moment, ρ = −0.09, p = 0.62). The sub-band

ratio I_{1670}/I_{1640} from Raman spectroscopy had a moderate, positive correlation with tissue strength ($\rho = 0.45$, $p = 0.01$) and modulus ($\rho = 0.54$, $p = 0.002$), but was not correlated with whole bone strength ($\rho = -0.10$, $p = 0.5$). Cortical porosity from SEM had a moderate, negative correlation with both tissue strength ($\rho = -0.38$, $p = 0.03$) and modulus ($\rho = -0.45$, $p = 0.01$), but these correlations were evident for males ($\rho = -0.57$, $p = 0.01$ for tissue strength, $\rho = -0.56$, $p = 0.02$ for modulus) and not so much for females ($\rho = 0.30$, $p = 0.31$ for strength, $\rho = 0.23$, $p = 0.42$ for modulus). Cortical porosity was not correlated with whole bone strength ($\rho = 0.19$, $p = 0.29$); however, when tested only in females, a weak correlation ($\rho = 0.30$, $p = 0.28$) between cortical porosity and whole bone strength was evident. We found no significant correlations between Ca_{Peak} and cortical porosity with bone fracture toughness (i.e., the critical stress intensity factor evaluated at the maximum load, Kc_{max}).

We found that local bone formation at the periosteal surface (Ps. MS/BS) was positively correlated with estimated bone tissue material properties including tissue strength ($\rho = 0.57$, $p = 0.002$) and modulus ($\rho = 0.36$, $p = 0.07$). Ps. MS/BS was not correlated with whole bone strength (i.e., peak bending moment, $\rho = 0.01$, $p = 0.93$). When tested only in females, Ps. MS/BS was positively correlated ($\rho = 0.57$, $p = 0.03$) with whole bone strength. Endocortical surface bone formation was not correlated ($\rho < 0.3$, $p > 0.05$) with whole bone mechanical or tissue material properties. Osteoclast number density from TRAP staining was not correlated with tissue strength ($\rho = 0.26$, $p = 0.15$) or modulus ($\rho = 0.25$, $p = 0.16$). Osteoclast number density had a weak negative correlation with whole bone strength ($\rho = -0.31$, $p = 0.09$), but this correlation was mainly evident for females ($\rho = -0.51$, $p = 0.06$) and not so much in males ($\rho = -0.15$, $p = 0.57$). We found no correlations between Ps. MS/BS and osteoclast number density with bone fracture toughness (i.e., critical stress intensity factor Kc_{max}) for pooled males and females. However, for females, we observed that bone fracture toughness positively correlated with Ps. MS/BS ($\rho = 0.66$, $p = 0.02$) and negatively correlated with osteoclast number density ($\rho = -0.43$, $p = 0.1$). These independent variables (i.e., collagen structure, cortical porosity, and bone turnover parameters) were not correlated or weakly correlated with each other ($\rho < 0.3$, $p > 0.05$), with the exception of osteoclast number density and cortical porosity, which displayed a negative correlation ($\rho = -0.46$, $p = 0.009$).

3.9 Microbiome and sex each distinctly influence the cortical bone metabolome

A total of 2,129 metabolite features were detected across all humerus cortical bone samples (Supplemental Table 3). We used PLS-DA to compare the effects of GF (GF vs. conventional), sex within treatment (GF males vs. GF females, conventional males vs. conventional females), and the effect of GF within sex (GF females vs. conventional females, GF males vs. conventional males). PLS-DA analysis of all four groups displayed minimal overlap, suggesting the metabolomes of all four groups were distinct (Figure 10A). Distinct separations were observed between male and female metabolites for GF mice (Figure 10B), GF males vs. conventional males (Figure 10C), and GF females vs. conventional females (Figure 10D).

Volcano plot analysis was utilized to identify sub-populations of metabolite features that were different between GF and conventional for mice of the same sex. In total, 152 features were statistically significant and had higher concentrations in GF females compared to conventional females, whereas 22 metabolite features were statistically significant and had higher concentrations in conventional females compared to GF females. (Figure 10E). 21 metabolite features were statistically significant and had higher concentrations in GF males compared to conventional males, whereas 188 were statistically significant and had higher concentrations in conventional males compared to GF males (Figure 10F).

Heatmap analysis identified clusters of metabolite features specific to the four groups of male and female GF and conventional mice (Figure 10G, Supplemental Table 3). Pathways associated with the selected clusters from heatmaps and with the metabolite features from the volcano plot were identified for each group. A shared metabolic theme among all females, GF and conventional, was increased levels of glycosaminoglycan degradation. The most significant metabolite feature for GF females was increased lipid metabolism (sphingolipid metabolism and arachidonic acid metabolism), whereas for conventional females, significant metabolite features corresponded to increased levels of glycosylphosphatidylinositol (GPI)-anchor biosynthesis and amino acid metabolism (cysteine, methionine). The shared metabolic theme among all males, GF and conventional, was increased levels of amino acid metabolism (alanine, aspartate, glutamate, arginine, histidine, cysteine, methionine). Metabolite features increased in GF males corresponded to increased levels of porphyrin metabolism, whereas features increased in conventional males corresponded to increased levels of purine metabolism, terpenoid backbone biosynthesis, and the pentose phosphate pathway.

4. Discussion

The purpose of this study was to test the hypothesis that GF C57BL/6J mice have increased bone mass and decreased bone fracture resistance compared to conventional mice. To test this hypothesis, we investigated the impact of GF status on bone tissue metabolism, bone turnover, bone matrix properties, microarchitecture, and whole bone fracture resistance. Our results demonstrate that GF mice have high bone mass and altered bone matrix compared to conventional mice, but not decreased fracture resistance (i.e., similar or higher strength and toughness). Our results also reveal important sex differences in the impact of GF on bone properties (Table 6).

Our results suggest the gut microbiome plays an important but different role in bone formation and resorption in female and male mice (Table 6). For both sexes, GF increased cortical bone formation at the femur diaphysis. GF females had reduced osteoclast density in cortical bone, but GF males did not. These cortical femur-specific data aligned with global serum biomarkers of bone formation and resorption. We observed no change in adipocyte density with GF, suggesting that mesenchymal stem cell differentiation toward adipocyte-lineage cells may not be influenced by GF status. GF mice have an immature immune system[19,25], which would be expected to influence precursors available for differentiation to osteoclasts. The presence of sexual dimorphism in immunological responses to different diseases has been previously reported, with greater pro-inflammatory

cytokine responses and T-cell proliferation in female humans and mice compared to their male counterparts[64,65]. Females also have enhanced innate and adaptive immune responses to inflammation or bacteria-driven diseases[66,67]. Similarly, evidence supports sex differences in osteoclast differentiation and precursor population, although specific results are contradictory[67-70]. Some studies reported that *in vitro* osteoclastogenesis occurs faster in osteoclast precursor derived from female mouse cells compared to male cells in the absence of pathogens[68,70], while others reported bacterial-induced osteoclastogenesis *in vitro* is faster in male osteoclast precursor cells compared to females[69]. The sex differences in the decline of osteoclast number in our study imply a likely difference in either the immune systems of male and female GF mice or a sexual dimorphism in the resilience of osteoclast differentiation on the immune system.

The osteocyte regulates bone remodeling[33,34], and prior work suggests that the osteoblast to osteocyte transition may be decreased in GF mice through disruptions in the immune system and bacteria-derived vitamin K_2 biosynthesis[30,71]. Therefore, we investigated the influences of GF and sex on osteocyte abundance, gene expression related to osteocyte control of osteoclast and osteoblast differentiation and lacunar-canalicular system turnover, and osteocyte perilacunar bone resorption. We found that GF status did not alter lacunar number density or percentage of empty lacunae for either females or males. GF increased RankL/OPG ratio by downregulating OPG expression in both males and females. The RankL-OPG signaling system regulates osteoclastogenesis in the marrow[72] and the downregulation of OPG promotes osteoclastogenesis and osteoclastic activity[73]. Osteocyte perilacunar bone resorption, as estimated from TRAP positive lacunae, was decreased with GF status. However, GF did not impact most measurements of gene expression related to lacunar-canalicular system remodeling. These data suggest efforts by osteocytes in the context of the GF model to decrease bone mass and participate in lacunar-canalicular bone remodeling but failure to achieve reduced osteoblast activity or increased osteoclast activity.

We observed that GF males and females had decreased whole bone strength (i.e., peak bending moment), increased bone tissue strength (i.e., ultimate stress) and modulus, and unchanged bone fracture toughness. Notably, our analysis to test the effect of GF vs. conventionally housed mice on critical stress intensity measured at maximum load (Kc_{max}) was underpowered in females, and it is possible that the addition of a few more bones (n=11 per group of females) could reveal an increase in Kc_{max} for GF females. GF mice had several disruptions to bone matrix, including increased cortical tissue mineralization from qBEI, increased fAGE content, and altered collagen structure as indicated by increased I_{1670}/I_{1640} and I_{1670}/I_{1610} ratios from Raman spectroscopy. However, we note that while fracture toughness has been shown in prior studies of human cortical bone to negatively correlate with amide I sub-band intensity ratios I_{1670}/I_{1640} and I_{1670}/I_{1610} [63], suggesting disrupted collagen structure[62,63], we do not witness this same relationship with GF mice.

It is currently unclear whether vitamin K plays a fundamental role in the strength and fracture toughness of bone tissue. The absent gut microbiome must necessarily eliminate the production of gut microbe-derived forms of vitamin K (menaquinones MK5-MK13, otherwise known as vitamin K_2)[71]. Vitamin K_2 directly impacts bone mineralization through carboxylation of osteocalcin, the most abundant non-collagenous protein[28,74-77].

Some reports also indicate that changes to osteocalcin mineralization can deleteriously affect fracture toughness[28,74,78,79]. We did not measure the vitamin K_2 content in study mice, but our data do not clearly support vitamin K_2 having a large effect on bone fracture resistance.

We sought to investigate whether the impacts of GF on estimated whole bone mechanical properties and tissue material properties were driven by cortical porosity or tissue mineralization. These independent variables were chosen because it is well-established that bone elastic modulus and strength correlate with bone cortical porosity[80-84] and tissue mineralization[82,84-88]. We found that whole bone strength (i.e., peak bending moment) was not correlated with cortical porosity or tissue mineralization from qBEI. However, both tissue strength (i.e., ultimate stress) and modulus had a weak-to-moderate positive correlation with tissue mineralization and a negative correlation with cortical porosity. These factors were also not intercorrelated ($\rho < 0.3$). Therefore, alterations in bone tissue strength and modulus with GF state are likely the result of multiple contributing factors including at least tissue mineralization and cortical porosity.

Because GF increased local bone formation (just Ps.MS/BS and not Ec.MS/BS) and decreased osteoclast number density, we also asked whether the changes to whole bone mechanical and tissue material properties were the results of decreased bone turnover. We found that whole bone strength (i.e., peak bending moment) did not correlate with local bone formation (Ps.MS/BS) nor with osteoclast number density in pooled male and female data. However, in females only, whole bone strength had a moderate positive correlation with Ps.MS/BS and a moderate negative correlation with osteoclast number density. Bone tissue strength (i.e., ultimate stress) and modulus for both sexes had a weak to moderate positive correlation with Ps.MS/BS but not with osteoclast number density. These results demonstrate that the impact of the gut microbiome on bone quality is partially, but not fully, determined by changes to bone turnover. Importantly, the lack of microbiome can cause several other important developmental differences in the skeleton compared to conventional mice. These differences include increased bone mass in growing C57BL/6 mice[19], shorter femurs in 7-week-old male BALB/c mice with smaller and thinner cortical area and lower bone volume fraction[89], and increased cortical thickness in 10-12 -week-old female C57BL/6 mice[20,21].

Since GF showed sex differences for some features of bone quality as well as in the abundance and activity of bone cells, we studied the sex differences in how GF affects bone cell metabolism. We evaluated the metabolism of cortical bone, which is predominantly populated by osteocytes. We found that compared to conventional mice of the same sex, female GF mice had increased lipid metabolism (highest of all groups) and male GF mice had differentially regulated metabolites in energy metabolism (i.e., upregulated porphyrin metabolism in GF males and upregulated purine metabolism in conventional males). Adipocyte number density was not increased in GF mice, suggesting that the increased levels of lipid metabolism are not a consequence of increased differentiation of mesenchymal stem cells to adipocytes. GF females also had increased levels of arachidonic acid metabolites, which are reported to be inhibitors of osteoclastic function, compared to conventional females [90]. Together, these findings suggest that osteoclast population and bone resorption activity in GF females could be impacted by altered dynamics of

lipid metabolism. Conversely, conventional females had increased levels of cysteine and its precursor methionine compared to GF females[91]. Cysteine is a key component of cathepsin k protease that is predominantly expressed in osteoclasts, and is essential to bone resorption activity[92]. Conventional females had the highest osteoclast population and global resorption activity among all groups, both of which drastically decreased with GF. Males had increased levels of energy and amino acid metabolisms compared to females, with GF males having the highest levels of porphyrin metabolism and conventional males having the highest levels of purine metabolism. This finding is consistent with GF males having the highest bone formation (P1NP and BV/TV) in all groups, based on our prior work[39]. We have previously reported that in conventional mice, bone cells from males and females rely on different metabolic pathways to meet their energy demands. While cells from male mice used amino acid metabolism, cells from females predominantly utilized lipid metabolism[39]. It appears that in GF mice, these differences between male and female cortical bone metabolome become even more pronounced. GF females and males both build more bone compared to conventional mice, but this evidence suggests that they may engage in different energy metabolism to do so. These results demonstrate that GF affects the bioenergetics of bone cells and that this impact is different in males and females.

A strength of our study is evaluating sex differences in multiscale bone quality for skeletally mature mice. Through this work, we have accumulated, to our knowledge, the largest dataset of sex differences in bone quality amongst conventional C57BL/6 mice currently available in the literature. Key differences pertaining to estimated whole bone mechanical and tissue material properties and microarchitecture include higher whole bone strength (peak bending moment), higher tissue strength (ultimate stress) and modulus, lower trabecular microstructure, and smaller cortical geometry in females compared to males. Sex differences related to bone turnover include increased bone mineralizing surface, higher bone turnover, decreased osteocyte perilacunar bone resorption, higher osteoclast number density, increased cathepsin K and MMP14 expression, and higher adipocyte number for females. Meanwhile, tissue-scale mineralization, collagen structure, and fAGE content were similar for conventional females and males. We anticipate that these reference data will be broadly useful in interpreting sex differences in bone quality occurring in disease models and other interventions.

Our study has several important limitations. First, GF mice have developmental differences with conventionally-raised mice[29,93], which likely have a confounding role in the effects of lack of microbiome on the skeleton. Second, it was necessary to characterize bone at multiple skeletal locations due to different sample preparation requirements for each technique, though skeletal site differences are likely to impact the reported results. A limitation in assessing bone tissue metabolism is that we cannot strictly discriminate which cells are responsible for the observed metabolism differences. Since osteocytes are the most common (>90%) cells in cortical bone[33,34], it is very likely that their metabolism is included in these metabolic shifts. However, it is possible that other cells present in the bone tissue (e.g., osteoblast, osteoblast, lining cells, possible remaining adipose cells) may contribute to the observed metabolomic differences between the groups as well. Another limitation of this study is that GF and conventional mice did not receive fully identical diets, although they had identical vitamin K content and a nearly identical percentage of

calories from protein, fat, and carbohydrates (Supplemental Table 2). We did not measure vitamin K content in the study animals, which limits our ability to test the relationship between vitamin K and changes to bone quality in the absence of the gut microbiome. Most importantly, GF models are not directly translatable to humans. Nonetheless, GF models provide unique insights about the origin of the microbiome impacts on the bone quality that are not accessible from other models. In this work, we did not investigate specific contributions of the gut microbiome to the regulation of bone matrix properties. Our findings motivate additional investigation in this area.

We conclude that the absence of the gut microbiome in female and male 20 to 21-week-old C57BL/6 mice not only increases bone mass but also impacts bone matrix properties, including collagen structure and bone mineralization. Notably, the absence of the gut microbiome does not decrease bone fracture resistance for GF mice (i.e., higher tissue strength and similar fracture toughness to conventional mice). Many repercussions of an absent gut microbiome on bone, such as the activities and abundance of remodeling bone cells, are sex-dependent. These alterations extend to the level of bone tissue metabolism as we demonstrate that GF exacerbates sex differences that are seen in conventionally-raised mice. This study advances the fundamental understanding of the gut microbiome and sex interactions and their effects on the development and maintenance of bone mass and matrix quality.

Supplementary Material

Refer to Web version on PubMed Central for supplementary material.

Acknowledgments

Data availability

Source mass spectrometry files are available on the Metabolomics Workbench repository under Study ID: ST002342.

References

1. Gordon JI. Honor thy gut symbionts redux. Science (1979). American Association for the Advancement of Science; 2012. p. 1251–3.

2. Markle JGM, Frank DN, Mortin-Toth S, Robertson CE, Feazel LM, Rolle-Kampczyk U, von Bergen M, Mccoy KD, Macpherson AJ, Danska JS. Sex Differences in the Gut Microbiome Drive Hormone-Dependent Regulation of Autoimmunity. Science (1979). 2013;339:1084–8.

3. Brettle H, Tran V, Drummond GR, Franks AE, Petrovski S, Vinh A, Jelinic M. Sex hormones, intestinal inflammation, and the gut microbiome: Major influencers of the sexual dimorphisms in obesity. Front Immunol. Frontiers Media SA; 2022 Sep 27;13.

4. Shi Y, Wei L, Xing L, Wu S, Yue F, Xia K, Zhang D. Sex Difference is a Determinant of Gut Microbes and Their Metabolites SCFAs/MCFAs in High Fat Diet Fed Rats. Curr Microbiol. NLM (Medline); 2022 Nov 1;79(11):347. [PubMed: 36209302]

5. Org E, Mehrabian M, Parks BW, Shipkova P, Liu X, Drake TA, Lusis AJ. Sex differences and hormonal effects on gut microbiota composition in mice. Gut Microbes. Taylor and Francis Inc.; 2016 Jul 3;7(4):313–22. [PubMed: 27355107]

6. Yurkovetskiy L, Burrows M, Khan AA, Graham L, Volchkov P, Becker L, Antonopoulos D, Umesaki Y, Chervonsky A v. Gender bias in autoimmunity is influenced by microbiota. Immunity. 2013 Aug 22;39(2):400–12. [PubMed: 23973225]

7. Kim YS, Unno T, Kim BY, Park MS. Sex differences in gut microbiota. World Journal of Men's Health. 2020;38(1):48–60.

8. Org E, Mehrabian M, Parks BW, Shipkova P, Liu X, Drake TA, Lusis AJ. Sex differences and hormonal effects on gut microbiota composition in mice. Gut Microbes. Taylor & Francis; 2016;7(4):313–22. [PubMed: 27355107]

9. Hernandez CJ, Guss JD, Luna M, Goldring SR. Links Between the Microbiome and Bone. Journal of Bone and Mineral Research. 2016;31(9):1638–46. [PubMed: 27317164]

10. Li J-Y, Jones RM, Pacifici R. Sex steroid deficiency – associated bone loss is microbiota dependent and prevented by probiotics. J Clin Invest. 2016;126(6):2049–63. [PubMed: 27111232]

11. Vijay-Kumar M, Aitken JD, Carvalho FA, Cullender TC, Mwangi S, Srinivasan S, Sitaraman SV, Knight R, Ley RE, Gewirtz AT. Metabolic syndrome and altered gut microbiota in mice lacking Toll-like receptor 5. Science (1979). American Association for the Advancement of Science; 2010;328(5975):228–31.

12. Pacifici R. T cells, osteoblasts, and osteocytes: interacting lineages key for the bone anabolic and catabolic activities of parathyroid hormone. Ann N Y Acad Sci. NIH Public Access; 2016;1364(1):11. [PubMed: 26662934]

13. Pacifici R Bone remodeling and the microbiome. Cold Spring Harb Perspect Med. Cold Spring Harbor Laboratory Press; 2018;8(4):a031203. [PubMed: 28847904]

14. Li Y, Toraldo G, Li A, Yang X, Zhang H, Qian WP, Weitzmann MN. B cells and T cells are critical for the preservation of bone homeostasis and attainment of peak bone mass in vivo. Blood. 2007;109(9):3839–48. [PubMed: 17202317]

15. Tyagi AM, Yu M, Darby TM, Vaccaro C, Li JY, Owens JA, Hsu E, Adams J, Weitzmann MN, Jones RM, Pacifici R. The Microbial Metabolite Butyrate Stimulates Bone Formation via T Regulatory Cell-Mediated Regulation of WNT10B Expression. Immunity. Cell Press; 2018 Dec 18;49(6):1116–1131.e7. [PubMed: 30446387]

16. Basu TK, Donaldson D. 6 Intestinal absorption in health and disease: micronutrients. Best Pract Res Clin Gastroenterol. 2003;17(6):957–79. [PubMed: 14642860]

17. Yan J, Takakura A, Zandi-Nejad K, Charles JF. Mechanisms of gut microbiota-mediated bone remodeling. Gut Microbes. 2018. p. 84–92. [PubMed: 28961041]

18. Michigami T. Paracrine and endocrine functions of osteocytes. Clinical Pediatric Endocrinology Review. 2023 Jan;32(1):1–10.

19. Sjögren K, Engdahl C, Henning P, Lerner UH, Tremaroli V, Lagerquist MK, Bäckhed F, Ohlsson C. The gut microbiota regulates bone mass in mice. Journal of Bone and Mineral Research. 2012;27(6):1357–67. [PubMed: 22407806]

20. Li JY, Yu M, Pal S, Tyagi AM, Dar H, Adams J, Neale Weitzmann M, Jones RM, Pacifici R. Parathyroid hormone-dependent bone formation requires butyrate production by intestinal microbiota. Journal of Clinical Investigation. American Society for Clinical Investigation; 2020 Apr 1;130(4):1767–81. [PubMed: 31917685]

21. Ohlsson C, Nigro G, Boneca IG, Bäckhed F, Sansonetti P, Sjögren K. Regulation of bone mass by the gut microbiota is dependent on NOD1 and NOD2 signaling. Cell Immunol. Elsevier; 2017;317(April):55–8. [PubMed: 28576260]

22. Hahn AK, Wallace CW, Welhaven HD, Brooks E, McAlpine M, Christiansen BA, Walk ST, June RK. The microbiome mediates epiphyseal bone loss and metabolomic changes after acute joint trauma in mice. Osteoarthritis Cartilage. Elsevier Ltd; 2021;29(6):882–93. [PubMed: 33744432]

23. Locantore P, Del Gatto V, Gelli S, Paragliola RM, Pontecorvi A. The Interplay between Immune System and Microbiota in Osteoporosis. Mediators Inflamm. Hindawi Limited; 2020;1–8.

24. Hrncir T, Stepankova R, Kozakova H, Hudcovic T, Tlaskalova-Hogenova H. Gut microbiota and lipopolysaccharide content of the diet influence development of regulatory T cells: Studies in germ-free mice. BMC Immunol. 2008 Nov 6;9.

25. Macpherson A drew J, Harris NL. Interactions between commensal intestinal bacteria and the immune system. Nat Rev Immunol. 2004;4(114):478–485. [PubMed: 15173836]

26. Novince CM, Whittow CR, Aartun JD, Hathaway JD, Poulides N, Chavez MB, Steinkamp HM, Kirkwood KA, Huang E, Westwater C, Kirkwood KL. Commensal Gut Microbiota Immunomodulatory Actions in Bone Marrow and Liver have Catabolic Effects on Skeletal Homeostasis in Health. Sci Rep. Nature Publishing Group; 2017 Dec 1;7(1).

27. Yan J, Herzog JW, Tsang K, Brennan CA, Bower MA, Garrett WS, Sartor BR, Aliprantis AO, Charles JF. Gut microbiota induce IGF-1 and promote bone formation and growth. Proc Natl Acad Sci U S A. 2016;113(47):E7554–63. [PubMed: 27821775]

28. Castaneda M, Strong JM, Alabi DA, Hernandez CJ. The Gut Microbiome and Bone Strength. Curr Osteoporos Rep. Current Osteoporosis Reports; 2020;677–83.

29. Yan J, Charles JF. Gut Microbiome and Bone: To Build, Destroy or Both? Physiol Behav. 2017;176(12):139–48. [PubMed: 28363838]

30. Atkins GJ, Welldon KJ, Wijenayaka AR, Bonewald LF, Findlay DM. Vitamin K promotes mineralization, osteoblast-to-osteocyte transition, and an anticatabolic phenotype by γ-carboxylation-dependent and -independent mechanisms. Am J Physiol Cell Physiol. 2009;297(6):1358–67.

31. Yamamoto H, Ramos-Molina B, Lick AN, Prideaux M, Albornoz V, Bonewald L, Lindberg I. Posttranslational processing of FGF23 in osteocytes during the osteoblast to osteocyte transition. Bone [Internet]. Elsevier Inc.; 2016;84:120–30. Available from: 10.1016/j.bone.2015.12.055 [PubMed: 26746780]

32. Zhang H, Majdeddin M, Gaublomme D, Taminiau B, Boone M, Elewaut D, Daube G, Josipovic I, Zhang K, Michiels J. 25-Hydroxycholecalciferol Reverses Heat Induced Alterations in Bone Quality in Finisher Broilers Associated With Effects on Intestinal Integrity and Inflammation. J Anim Sci Biotechnol. Journal of Animal Science and Biotechnology; 2021;12(1):1–21. [PubMed: 33397465]

33. Bonewald LF. The amazing osteocyte. Journal of bone and mineral research. Wiley Online Library; 2011;26(2):229–38. [PubMed: 21254230]

34. Schaffler MB, Cheung WY, Majeska R, Kennedy O. Osteocytes: Master orchestrators of bone. Calcif Tissue Int. 2014;94(1):5–24. [PubMed: 24042263]

35. Tiede-Lewis LM, Hulbert MA, Campos R, Dallas MR, Bonewald LF, Dallas SL. Degeneration of the osteocyte network in the C57Bl/6 mouse model of aging. Aging. 2017;9(10):2190–208. [PubMed: 29074822]

36. Toth Z, Ward A, Tang SY, McBride-Gagyi S. Sexual differences in bone porosity, osteocyte density, and extracellular matrix organization due to osteoblastic-specific Bmp2 deficiency in mice. Bone. Elsevier Inc.; 2021 Sep 1;150.

37. Dole NS, Yee CS, Mazur CM, Acevedo C, Alliston T. TGFβ Regulation of Perilacunar/Canalicular Remodeling Is Sexually Dimorphic. Journal of Bone and Mineral Research. 2020;35(8):1549–61. [PubMed: 32282961]

38. Tremaroli V, Bäckhed F. Functional interactions between the gut microbiota and host metabolism. Nature. 2012;489(7415):242–9. [PubMed: 22972297]

39. Welhaven HD, Vahidi G, Walk ST, Bothner B, Martin SA, Heveran CM, June RK. The Cortical Bone Metabolome of C57BL / 6J Mice Is Sexually Dimorphic . JBMR Plus. Wiley; 2022 Jul 22;6(7):10654.

40. Fontaine CA, Skorupski AM, Vowles CJ, Anderson NE, Poe SA, Eaton KA. How free of germs is germ-free? Detection of bacterial contamination in a germ free mouse unit. Gut Microbes. 2015;6(4):225–33. [PubMed: 26018301]

41. Bouxsein ML, Boyd SK, Christiansen BA, Guldberg RE, Jepsen KJ, Müller R. Guidelines for assessment of bone microstructure in rodents using micro–computed tomography. Journal of bone and mineral research. Wiley Online Library; 2010;25(7):1468–86. [PubMed: 20533309]

42. Turner CH, Burr DB. Basic biomechanical measurements of bone: A tutorial. Bone. 1993;14(4):595–608. [PubMed: 8274302]

43. Ritchie RO, Koester KJ, Ionova S, Yao W, Lane NE, Ager JW. Measurement of the toughness of bone: A tutorial with special reference to small animal studies. Bone. Elsevier B.V.; 2008;43(5):798–812. [PubMed: 18647665]

44. Chudoba T, Richter F. Investigation of creep behaviour under load during indentation experiments and its influence on hardness and modulus results. Surf Coat Technol. Elsevier; 2001;148(2–3):191–8.

45. Oliver WC, Pharr GM. An improved technique for determining hardness and elastic modulus using load and displacement sensing indentation experiments. J Mater Res. Cambridge University Press; 1992;7(6):1564–83.

46. Campbell SE, Ferguson VL, Hurley DC. Nanomechanical mapping of the osteochondral interface with contactresonance force microscopy and nanoindentation. Acta Biomater. Acta Materialia Inc.; 2012;8(12):4389–96. [PubMed: 22877818]

47. Boyde A, Travers R, Glorieux FH, Jones SJ. The mineralization density of iliac crest bone from children with osteogenesis imperfecta. Calcif Tissue Int. 1999;64(3):185–90. [PubMed: 10024373]

48. Heveran CM, Ortega AM, Cureton A, Clark R, Livingston EW, Bateman TA, Levi M, King KB, Ferguson VL. Moderate chronic kidney disease impairs bone quality in C57Bl/6J mice. Bone. 2016;86:1–9. [PubMed: 26860048]

49. Campbell SE, Geiss RH, Feller SA, Ferguson VL. Tunable glass reference materials for quantitative backscattered electron imaging of mineralized tissues. J Mater Res. 2012;27(19):2568–77.

50. Roschger P, Fratzl P, Eschberger J, Klaushofer K. Validation of quantitative backscattered electron imaging for the measurement of mineral density distribution in human bone biopsies. Bone. 1998;23(4):319–26. [PubMed: 9763143]

51. Unal M, Jung H, Akkus O. Novel Raman Spectroscopic Biomarkers Indicate That Postyield Damage Denatures Bone's Collagen. Journal of Bone and Mineral Research. 2016;31(5):1015–25. [PubMed: 26678707]

52. Unal M, Ahmed R, Mahadevan-Jansen A, Nyman JS. Compositional assessment of bone by Raman spectroscopy. Analyst. 2021;146(24):7444–70.

53. Unal M, Akkus O. Raman spectral classification of mineral- and collagen-bound water's associations to elastic and post-yield mechanical properties of cortical bone. Bone. Elsevier B.V.; 2015;81:315–26. [PubMed: 26211992]

54. Vashishth D, Gibson GJ, Khoury JI, Schaffler MB, Kimura J, Fyhrie DP. Influence of nonenzymatic glycation on biomechanical properties of cortical bone. Bone. Elsevier; 2001;28(2):195–201. [PubMed: 11182378]

55. Viguet-Carrin S, Farlay D, Bala Y, Munoz F, Bouxsein ML, Delmas PD. An in vitro model to test the contribution of advanced glycation end products to bone biomechanical properties. Bone. Elsevier; 2008;42(1):139–49. [PubMed: 17974517]

56. Karim L, Moulton J, van Vliet M, Velie K, Robbins A, Malekipour F, Abdeen A, Ayres D, Bouxsein ML. Bone microarchitecture, biomechanical properties, and advanced glycation end-products in the proximal femur of adults with type 2 diabetes. Bone. Elsevier; 2018;114:32–9. [PubMed: 29857063]

57. Merlo K, Aaronson J, Vaidya R, Rezaee T, Chalivendra V, Karim L. In Vitro-Induced High Sugar Environments Deteriorate Human Cortical Bone Elastic Modulus and Fracture Toughness. Journal of Orthopaedic Research®. Wiley Online Library; 2020;38(5):972–83. [PubMed: 31793028]

58. Tang SY, Zeenath U, Vashishth D. Effects of non-enzymatic glycation on cancellous bone fragility. Bone. Elsevier; 2007;40(4):1144–51. [PubMed: 17257914]

59. Gross J Studies on the formation of collagen: I. Properties and fractionation of neutral salt extracts of normal guinea pig connective tissue. J Exp Med. The Rockefeller University Press; 1958;107(2):247. [PubMed: 13491760]

60. Carlson AK, Rawle RA, Adams E, Greenwood MC, Bothner B, June RK. Application of global metabolomic profiling of synovial fluid for osteoarthritis biomarkers. Biochem Biophys Res Commun. 2018 May;499(2):182–8. [PubMed: 29551687]

61. Jutila AA, Zignego DL, Hwang BK, Hilmer JK, Hamerly T, Minor CA, Walk ST, June RK. Candidate mediators of chondrocyte mechanotransduction via targeted and untargeted metabolomic measurements. Arch Biochem Biophys. Elsevier Inc.; 2014;545:116–23. [PubMed: 24440608]

62. Unal M, Jung H, Akkus O. Novel Raman Spectroscopic Biomarkers Indicate That Postyield Damage Denatures Bone's Collagen. Journal of Bone and Mineral Research. 2016;31(5):1015–25. [PubMed: 26678707]

63. Unal M, Uppuganti S, Timur S, Mahadevan-Jansen A, Akkus O, Nyman JS. Assessing matrix quality by Raman spectroscopy helps predict fracture toughness of human cortical bone. Sci Rep. Nature Publishing Group; 2019 Dec 1;9(1).

64. Fish Eleanor N.. The X-files in immunity: sex-based differences predispose immune responses. Nat Rev Immunol. 2008;8:737–44. [PubMed: 18728636]

65. Klein SL, Flanagan KL. Sex differences in immune responses. Nat Rev Immunol. Nature Publishing Group; 2016. p. 626–38.

66. Jaillon S, Berthenet K, Garlanda C. Sexual Dimorphism in Innate Immunity. Clin Rev Allergy Immunol. Humana Press Inc.; 2019. p. 308–21.

67. Valerio MS, Kirkwood KL. Sexual Dimorphism in Immunity to Oral Bacterial Diseases: Intersection of Neutrophil and Osteoclast Pathobiology. J Dent Res. SAGE Publications Inc.; 2018. p. 1416–23.

68. Mun SH, Jastrzebski S, Kalinowski J, Zeng S, Oh B, Bae S, Eugenia G, Khan NM, Drissi H, Zhou P, Shin B, Lee S-K, Lorenzo J, Park-Min K-H. Sexual Dimorphism in Differentiating Osteoclast Precursors Demonstrates Enhanced Inflammatory Pathway Activation in Female Cells. Journal of Bone and Mineral Research. 2021;36(6):1104–16. [PubMed: 33567098]

69. Valerio MS, Basilakos DS, Kirkpatrick JE, Chavez M, Hathaway-Schrader J, Herbert BA, Kirkwood KL. Sex-based differential regulation of bacterial-induced bone resorption. J Periodontal Res. Blackwell Munksgaard; 2017 Jun 1;52(3):377–87. [PubMed: 27509894]

70. Delahunty KM, Shultz KL, Gronowicz GA, Koczon-Jaremko B, Adamo ML, Horton LG, Lorenzo J, Donahue LR, Ackert-Bicknell C, Kream BE, Beamer WG, Rosen CJ. Congenic mice provide in Vivo evidence for a genetic locus that modulates serum insulin-like growth factor-I and bone acquisition. Endocrinology. 2006;147(8):3915–23. [PubMed: 16675518]

71. Guss JD, Taylor E, Rouse Z, Roubert S, Higgins CH, Thomas CJ, Baker SP, Vashishth D, Donnelly E, Shea MK, Booth SL, Bicalho RC, Hernandez CJ. The microbial metagenome and bone tissue composition in mice with microbiome-induced reductions in bone strength. Bone. 2019;127(May):146–54. [PubMed: 31207357]

72. Pathak JL, Bravenboer N, Luyten FP, Verschueren P, Lems WF, Klein-Nulend J, Bakker AD. Mechanical loading reduces inflammation-induced human osteocyte-to-osteoclast communication. Calcif Tissue Int. Springer US; 2015;97(2):169–78. [PubMed: 25967362]

73. Boyle WJ, Simonet WS, Lacey DL. Osteoclast differentiation and activation. 2003;423(May):337–42.

74. Poundarik AA, Diab T, Sroga GE, Ural A, Boskey AL, Gundberg CM, Vashishth D. Dilatational band formation in bone. Proceedings of the National Academy of Sciences. National Acad Sciences; 2012;109(47):19178–83.

75. Poundarik AA, Boskey A, Gundberg C, Vashishth D. Biomolecular regulation, composition and nanoarchitecture of bone mineral. Sci Rep. Springer US; 2018;8(1):1–8. [PubMed: 29311619]

76. Hauschka P v Lian JB, Gallop PM. Direct identification of the calcium-binding amino acid, y-carboxyglutamate, in mineralized tissue. 1975;72(10):3925–9.

77. Gundberg CM, Lian JB, Booth SL. Vitamin K-dependent carboxylation of osteocalcin: Friend or foe? Advances in Nutrition. 2012. p. 149–57. [PubMed: 22516722]

78. Nikel O, Poundarik AA, Bailey S, Vashishth D. Structural role of osteocalcin and osteopontin in energy dissipation in bone. J Biomech. Elsevier Ltd; 2018 Oct 26;80:45–52. [PubMed: 30205977]

79. Inaba N, Sato T, Yamashita T. Low-Dose Daily Intake of Vitamin K 2 (Menaquinone-7) Improves Osteocalcin g-Carboxylation: A Double-Blind, Randomized Controlled Trials. J Nutr Sci Vitaminol. 2015;61:471–80. [PubMed: 26875489]

80. Cooper DML, Kawalilak CE, Harrison K, Johnston BD, Johnston JD. Cortical Bone Porosity: What Is It, Why Is It Important, and How Can We Detect It? Curr Osteoporos Rep. Current Medicine Group LLC 1; 2016. p. 187–98.

81. Augat P, Reeb H, Claes LE. Prediction of fracture load at different skeletal sites by geometric properties of the cortical shell. Journal of Bone and Mineral Research. Wiley Online Library; 1996;11(9):1356–63. [PubMed: 8864911]

82. Currey JD. The effect of porosity and mineral content on the Young's modulus of elasticity of compact bone. J. Biomechics. 1988;21(2):131–9.

83. Currey J Incompatible mechanical properties in compact bone. J Theor Biol. 2004 Dec 21;231(4):569–80. [PubMed: 15488534]

84. Schaffler MB, Burr DB. Stiffness of compact bone: effects of porosity and density. 1988.

85. Hernandez CJ, Beaupré GS, Keller TS, Carter DR. The Influence of Bone Volume Fraction and Ash Fraction on Bone Strength and Modulus. Bone. 2001;29(1):74–8. [PubMed: 11472894]

86. Boivin GY, Chavassieux PM, Santora AC, Yates J, Meunier PJ. Alendronate Increases Bone Strength by Increasing the Mean Degree of Mineralization of Bone Tissue in Osteoporotic Women. Bone. 2000;27(5):687–94. [PubMed: 11062357]

87. Vose GP, Kubala AL. Bone strength-its relationship to x-ray-determined ash content. Hum Biol. Human Biology; 1959;31(3):261–70.

88. Currey JD. Strain rate and mineral content in fracture models of bone. Journal of Orthopaedic Research. 1988;6(1):32–8. [PubMed: 3334737]

89. Schwarcz HP, McNally EA, Botton GA. Dark-field transmission electron microscopy of cortical bone reveals details of extrafibrillar crystals. J Struct Biol. Elsevier Inc.; 2014;188(3):240–8. [PubMed: 25449316]

90. Fuller K, Chambers TJ. Effect of arachidonic acid metabolites on bone resorption by isolated rat osteoclasts. Journal of Bone and Mineral Research. 1989;4(2):209–15. [PubMed: 2499165]

91. Castellano R, Perruchot MH, Tesseraud S, Métayer-Coustard S, Baeza E, Mercier Y, Gondret F. Methionine and cysteine deficiencies altered proliferation rate and time-course differentiation of porcine preadipose cells. Amino Acids. Springer-Verlag Wien; 2017 Feb 1;49(2):355–66. [PubMed: 27888346]

92. Lu J, Wang M, Wang Z, Fu Z, Lu A, Zhang G. Advances in the discovery of cathepsi. inhibitors on bone resorption. J Enzyme Inhib Med Chem. Taylor and Francis Ltd; 2018. p. 890–904.

93. Niimi K, Takahashi E. New system to examine the activity and water and food intake of germ-free mice in a sealed positive-pressure cage. Heliyon. 2019;5(8):e02176. [PubMed: 31463382]
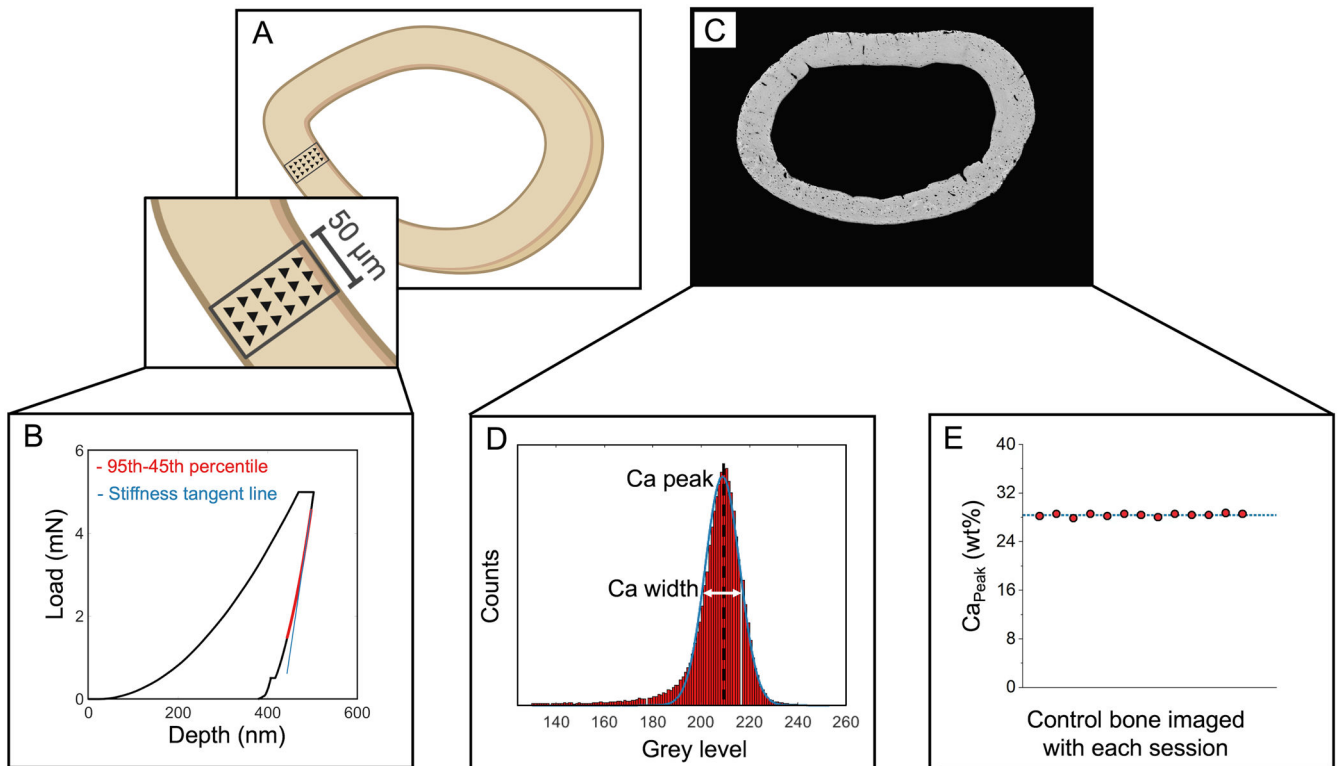
Figure 1.
Tissue-scale characterization of the cortical femur mid-diaphysis. A) Tissue-scale modulus
was assessed in maps spanning the cortical thickness in the posterior quadrant.
B) Representative load-displacement curve from a nanoindentation test. C) Tissue
mineralization was evaluated using quantitative backscattered electron microscopy. D)
Ca_{Peak} and Ca_{Width} were calculated from histograms of each femur cross-section. E) In
addition to the use of reference standards, one control bone sample was evaluated with each
imaging session. There was 0.85% variation in the Ca_{Peak} for the control bone measured
across imaging sessions.

Figure 2.
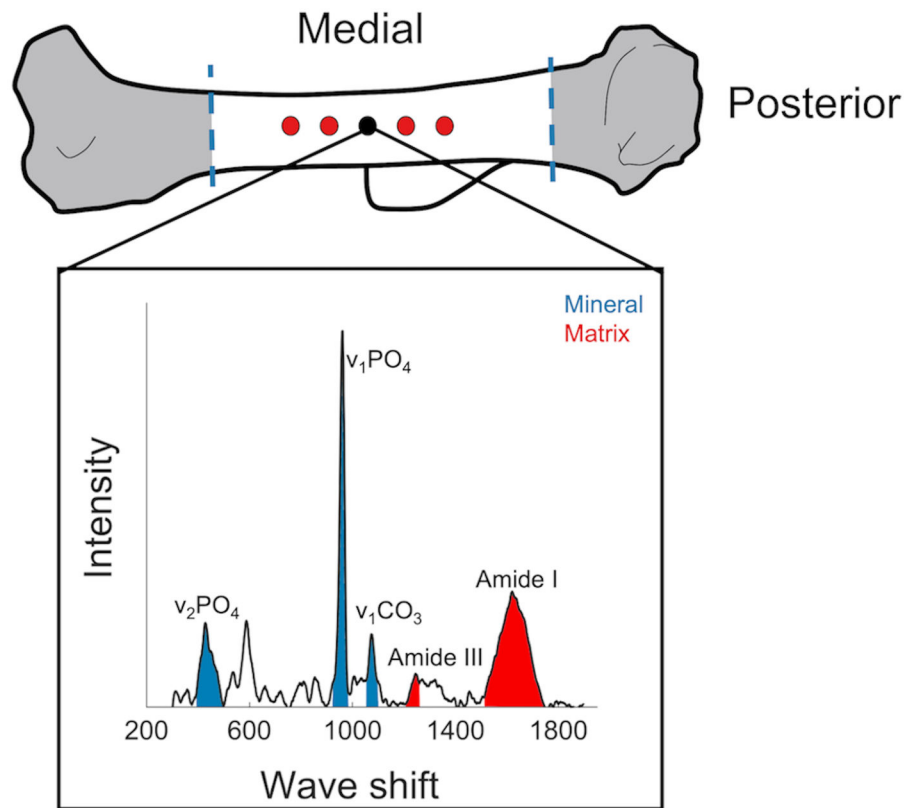Raman spectroscopy of hydrated humeri. Spectra were collected from five points on the posterior side of the humeri. The first point (colored black) was located where the deltoid tuberosity connects to the posterior, and other points were located 50 μm apart spanning both directions.
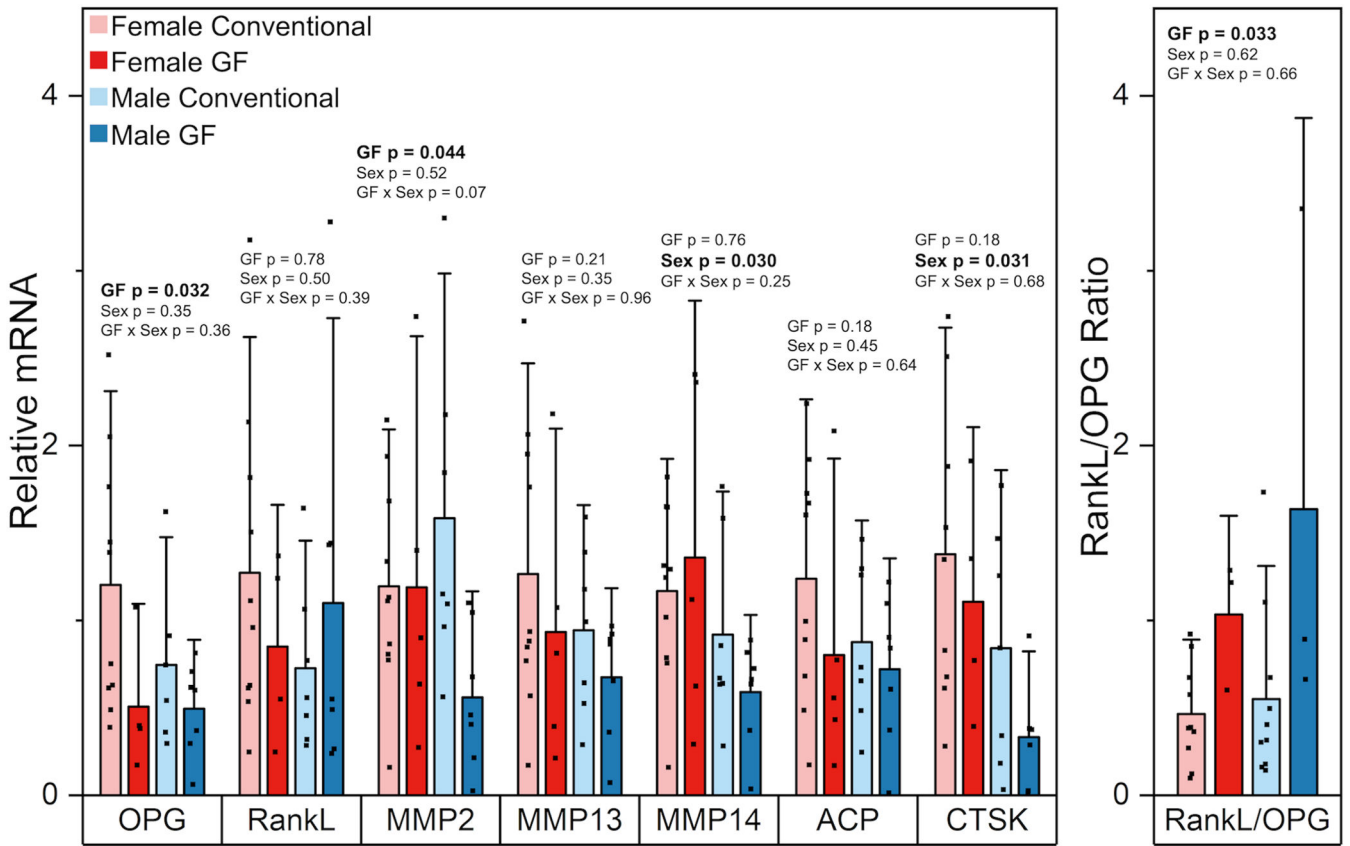
Figure 3.

Effects of GF and sex on relative gene expression levels (fold changes) of OPG, RankL, MMP2, MMP13, MMP14, ACP, CTSK, and on the non-relative expression level of RankL/OPG ratio. OPG expression was lower in GF mice compared to conventional mice. RankL expression was similar among groups. MMP2 expression decreased with GF. MMP13 expression was similar among groups. MMP14 was expressed more in females compared to males but was unchanged with GF. ACP5 did not differ with sex or GF. CTSK expression was lower in females than males but not changed with GF. The RankL/OPG ratio was higher in GF mice compared to conventional mice. Data are presented as means. Error bars indicate one standard deviation. P-values for significant main effects of GF or sex are shown above each gene. All p-values correspond with results of the omnibus ANOVA test. There were no interactions between sex and GF.
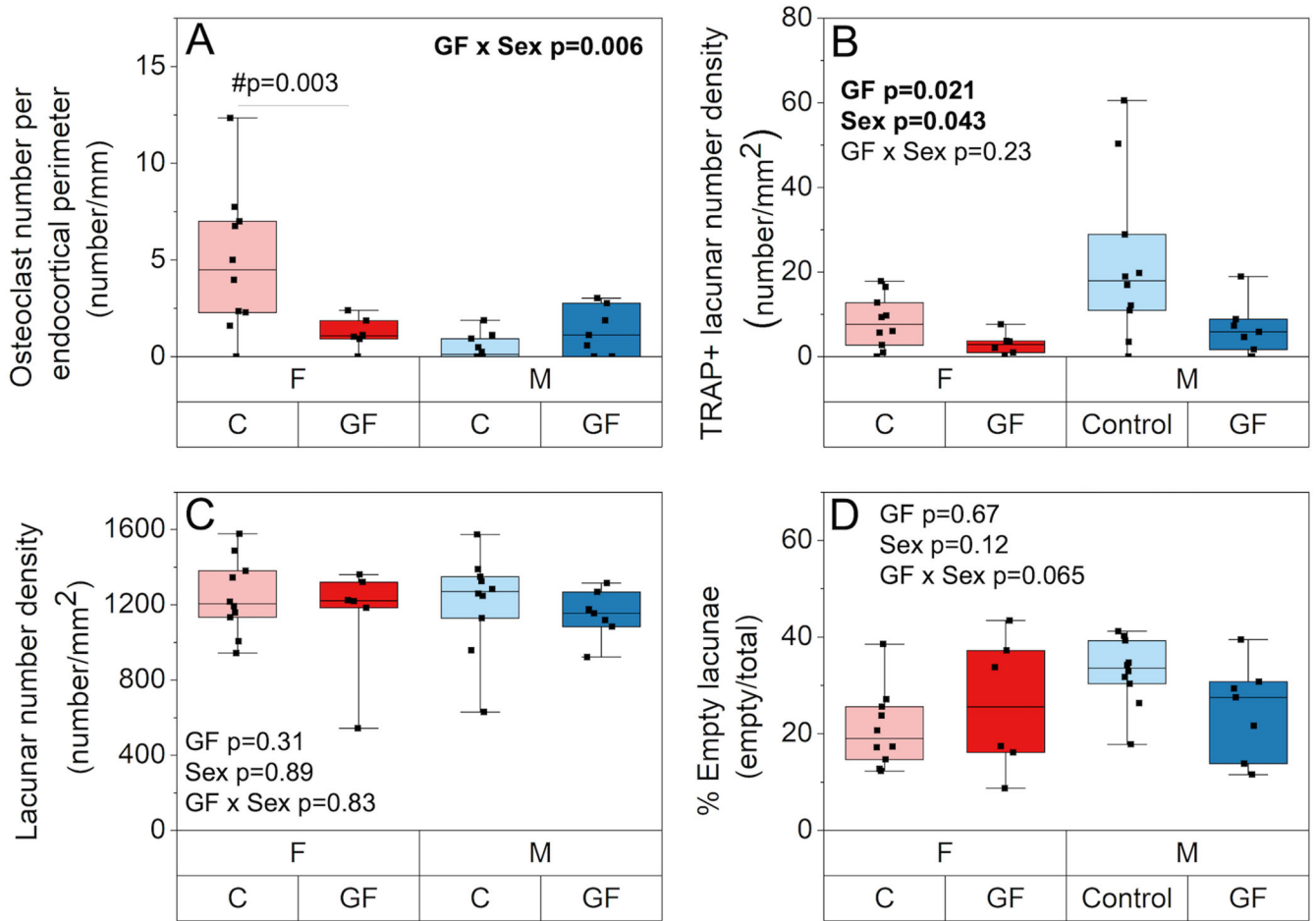
Figure 4.
The effect of GF and sex on bone resorbing cells. A) Sex and GF had an interactive effect on osteoclast number density per perimeter (number/mm), such that only GF females had reduced osteoclasts per endocortical perimeter compared to their conventional mice. B) TRAP-stained osteocyte lacunar number density per area (number/mm^2) was decreased in females and GF overall. C) lacunar number density per area (number/mm^2) and D) percent empty lacunae were not influenced by microbiome status or sex. Boxplots represent median value (cross), interquartile range (box), minimum/maximum (whiskers), and symbols representing all data points. All p-values correspond with results of the omnibus ANOVA test, unless specifically indicated with symbol # which indicates a pairwise post-hoc test following a significant interaction.

Figure 5.

The effect of GF and sex on serum biomarkers of bone turnover. A) P1NP, a biomarker of global bone formation, was higher in GF mice compared to conventional mice and in males compared to females. B) CTX1, a biomarker of global bone resorption, had a significant interaction between GF and sex such that CTX1 level was similar among GF and conventional males but lower and more homogenous in GF females compared with conventional females. C) CTX1/P1NP ratio was lower with GF in both sexes and was also higher in females compared to males. Boxplots represent median value (cross), interquartile range (box), minimum/maximum (whiskers), and symbols representing all data points. All p-values correspond with results of the omnibus ANOVA test, unless specifically indicated with symbol # which indicates a pairwise post-hoc test following a significant interaction.

Figure 6.
Cortical porosity assessments. A) Total porosity was decreased for GF males compared to conventional males but was unchanged in females. B) Lacunar porosity, C) vascular porosity, and D) pore number density were unchanged with sex and GF. Boxplots represent median value (cross), interquartile range (box), minimum/maximum (whiskers), and symbols representing all data points. All p-values correspond with results of the omnibus ANOVA test, unless specifically indicated with symbol # which indicates a pairwise post-hoc test following a significant interaction.
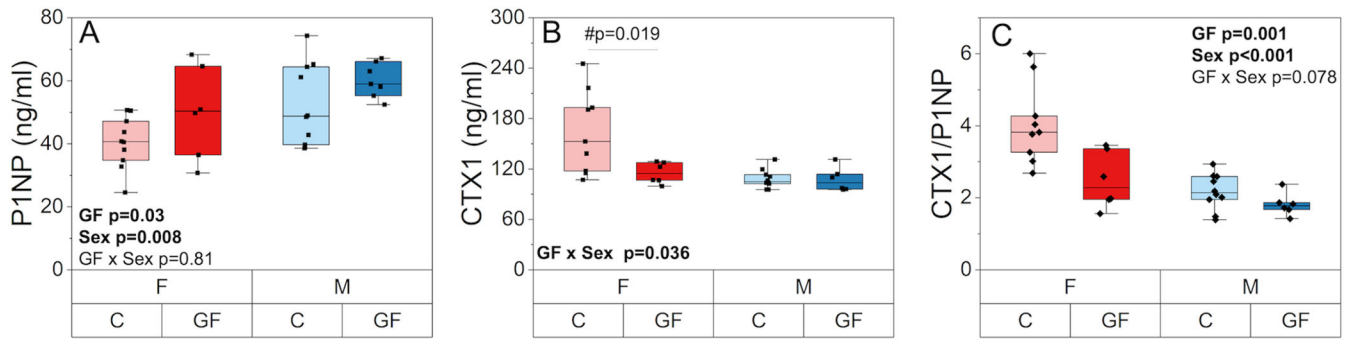
Figure 7.
Whole bone and tissue properties of femurs for GF versus conventional mice from flexural testing. A) The linear relationship between whole bone strength (peak bending moment) and section modulus was altered with GF in female mice but not males. B) I_{min} is increased for GF females and decreased for GF males compared with conventional mice of the same sex. C) Tissue strength (i.e., ultimate stress) and D) modulus were greater for GF compared with conventional mice of both sexes. E) Kc_{max} from notched fracture testing of the contralateral femur did not differ with GF or sex but may be underpowered for females (GF females vs. conventional females, p = 0.1). Boxplots represent median (cross), interquartile range (box), minimum/maximum (whiskers), and symbols representing all data points. All p-values correspond with results of the omnibus ANOVA test, unless specifically indicated with symbol # which indicates a pairwise post-hoc test following a significant interaction.
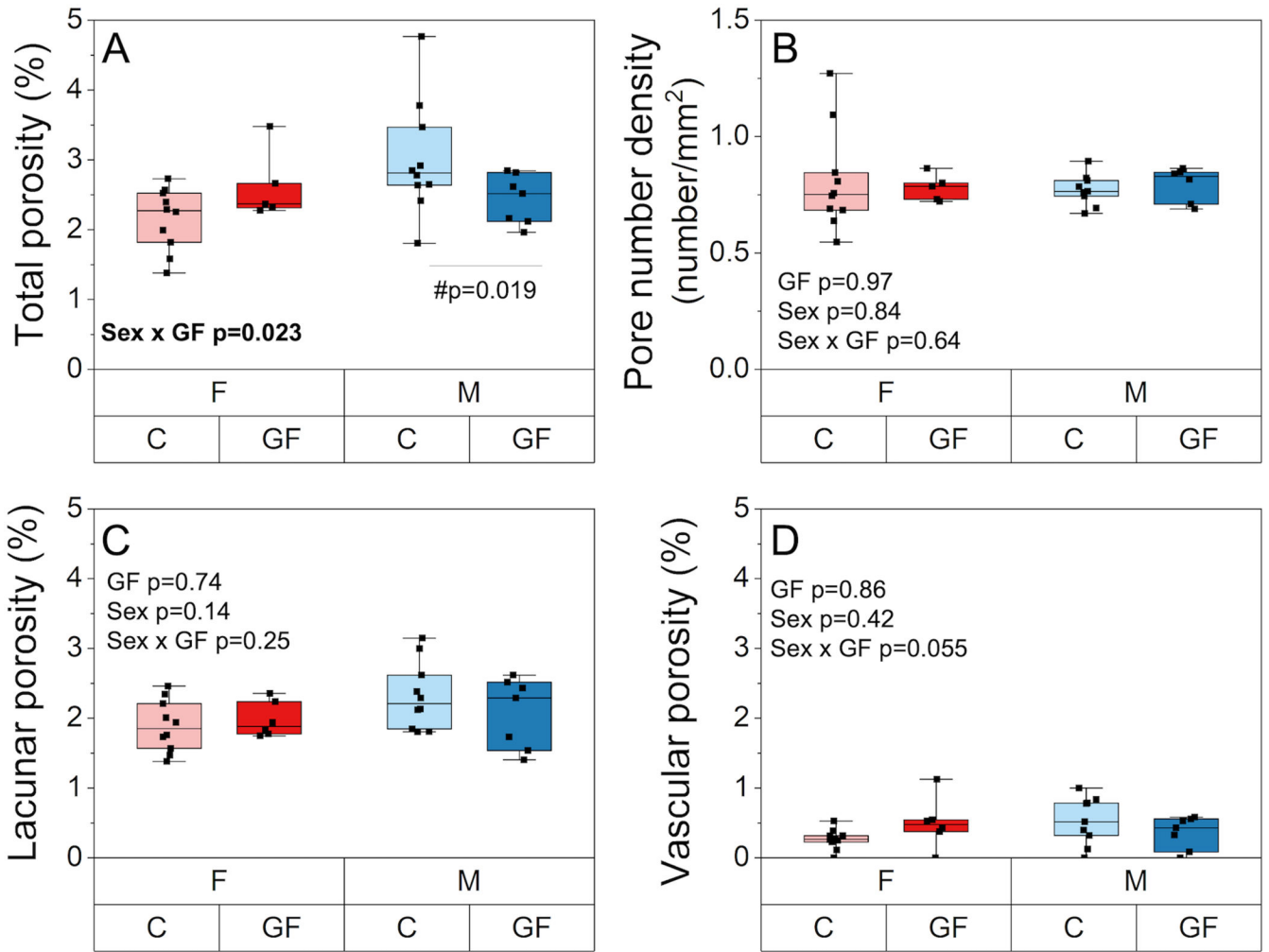
Figure 8.
The effect of GF and sex on tissue scale composition and collagen structure. A) Mineral-to-matrix ratio was higher in GF mice compared to conventional mice for both sexes. B) Carbonate to phosphate ratio was not affected by Gf or sex. C) I_{1670}/I_{1640} ratio and D) I_{1670}/I_{1610} ratio were increased with GF. Boxplots represent median value (cross), interquartile range (box), minimum/maximum (whiskers), and symbols representing all data points. All p-values correspond with results of the omnibus ANOVA test.
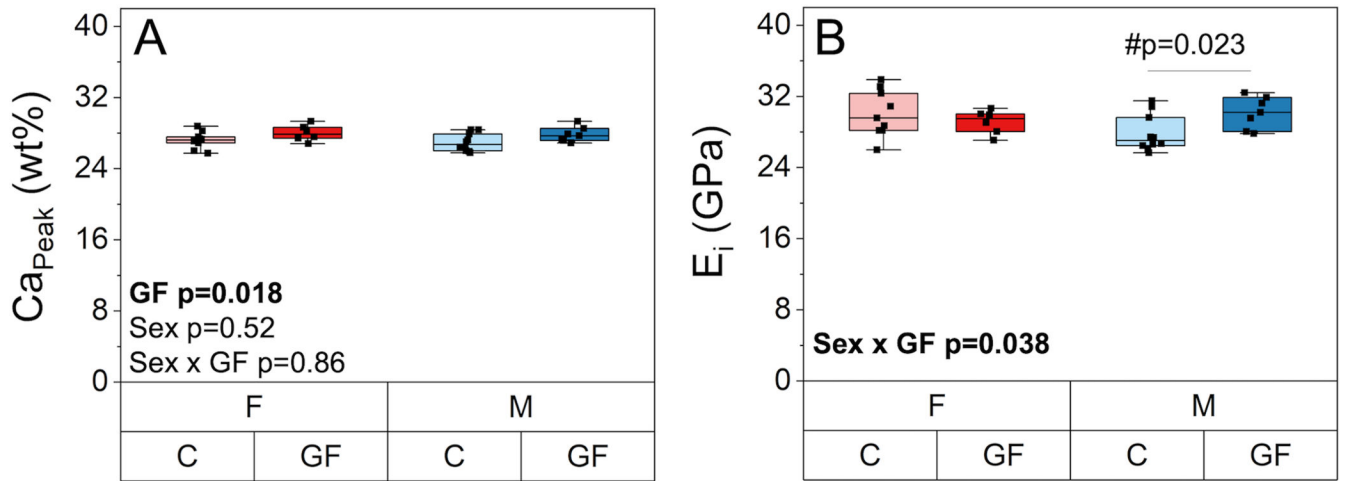
Figure 9.

The effect of GF and sex on tissue scale material properties. A) Ca$_{Peak}$ from qBEI was slightly higher with GF but was not affected by sex. B) Nanoindentation modulus (E$_i$) was increased in GF males and was unchanged in GF females compared to their respective conventional groups. Boxplots represent median value (cross), interquartile range (box), minimum/maximum (whiskers), and symbols representing all data points. All p-values correspond with results of the omnibus ANOVA test, unless specifically indicated with symbol # which indicates a pairwise post-hoc test following a significant interaction.
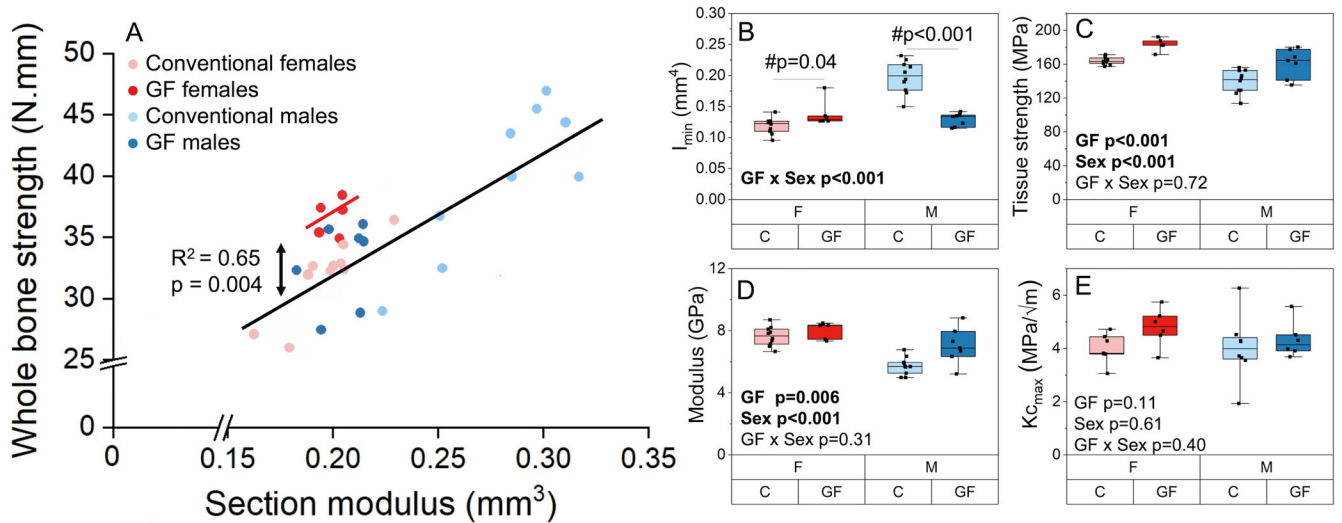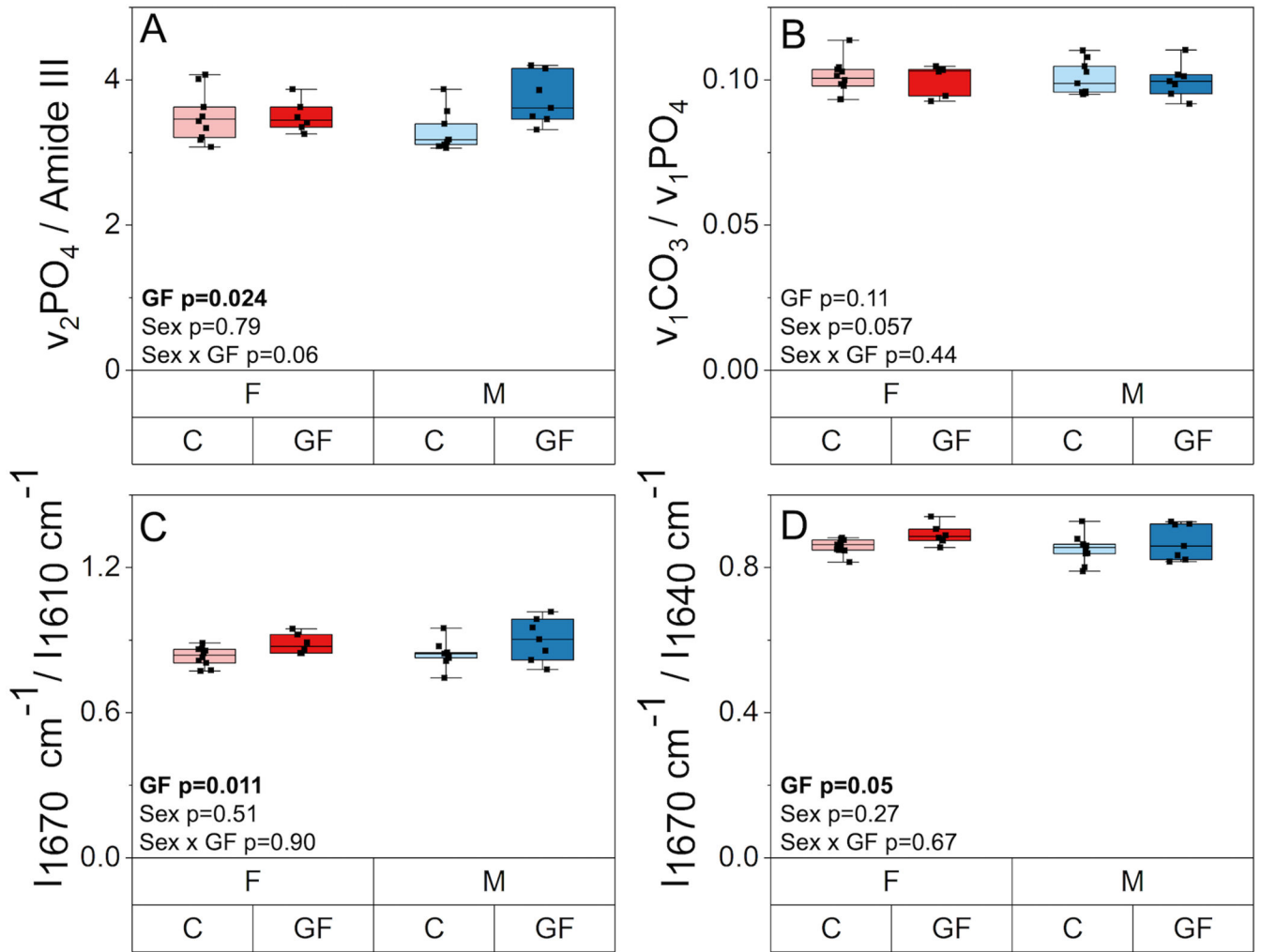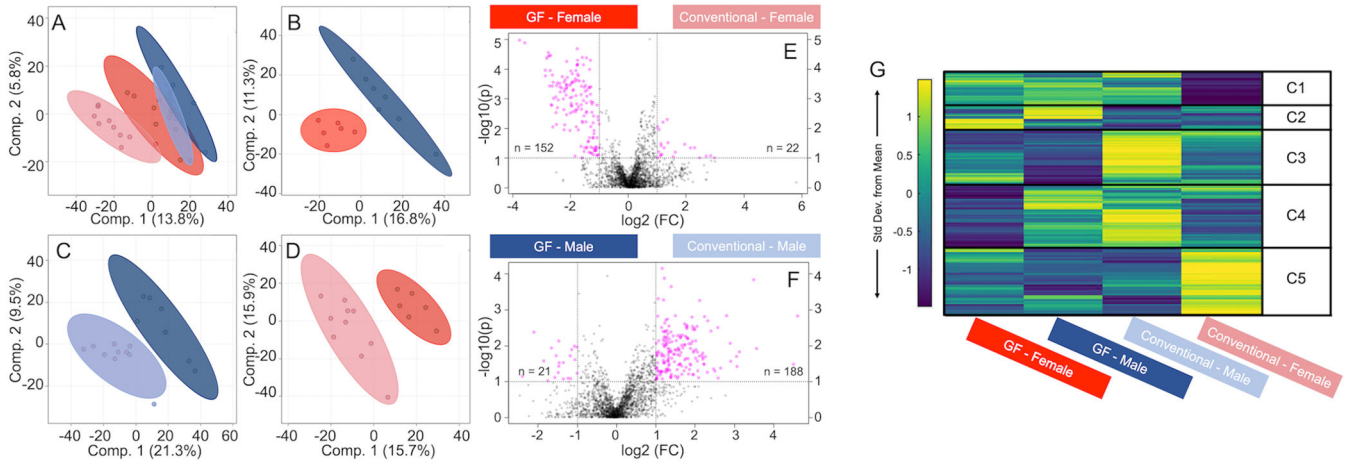
Figure 10.
Global metabolomic profiles of humeri-derived cortical bone vary by sex and microbiome, as identified by multiple analyses. From supervised PLS-DA analysis, A) metabolites of all four groups showed a clear separation. B) GF males and GF females, C) GF males and conventional males, and D) GF females and conventional females all had distinct metabolomes. From volcano plot analysis (E) metabolite features detected for GF females were significantly different from the ones detected for conventional females, and similarly (F) metabolite features were differently regulated between GF males and conventional males. (G) Median intensity heatmap analysis displayed clusters of metabolites that are differentially regulated between all groups. C1-C5 = clusters 1 – 5.

Table 1.

Literature review of the effects of germ-free (GF) status on hindlimb bone quality. Arrows directions are in reference to the effect of GF versus conventionally raised mice.

Study	Mouse model	Bone measurement	Key findings	
Sjögren et al., "The gut microbiota regulates bone mass in mice", JBMR, 2012.[19]	Female C57BL/6J 7-9 weeks old	pQCT, microCT, histomorphometry	*Proximal tibia metaphysis*	*at 7 weeks:*
			vBMD	↑ 3.2%
			Femur diaphysis	*at 9 weeks:*
			Ct. Area	↑ 8.9%
			Distal femur metaphysis	*at 7 weeks*
			BV/TV	↑ 39.7%
			Tb.N	↑ 36.%
			Tb.Sp	↓ 29.2%
			Tb.Th	≈
			Distal femur metaphysis	*at 9 weeks*
			MAR	≈
			M.S/Tb.S	↑ 17.0%
			N.Oc/BS	↓ 11.0%
			TRAP+ Oc.N (> 5 nuclei)	↓ 57.8% (at 8 weeks)
Schwarzer et al., "Lactobacillus plantarum strain maintains growth of infant mice during chronic undernutrition", Science, 2016.[69]	Male BALB/c 7 weeks old	MicroCT	*Femur length*	↓ 3.09%
			Femur diaphysis	
			Ct.Th	↓ ~9.6%
			Ct.Ar./Tt.Ar	↓ ~4.7%
			Ct.BMD	≈
			Distal femur metaphysis	
			BV/TV	↓ ~24.6%
Li et al., "Sex steroid deficiency–associated bone loss is microbiota dependent and prevented by probiotics", JCI, 2016.[10]	Female C57BL/6J 20 weeks old	MicroCT	*Femur metaphysis*	
			BV/TV	↑ ~25%
			Tb.N	↑ ~30%
			Tb.Sp	↓ ~24%
			Tb.Th	≈
			Femur diaphysis	
			Ct.Vol	↑ ~6%
			Ct.Th	↑ ~10%
Li et al., "Parathyroid hormone–dependent bone formation requires butyrate production by intestinal microbiota", JCI, 2020.[20]	Female C57BL/6 12 weeks old	MicroCT, histomorphometry	*Femur metaphysis*	
			BV/TV	≈
			Tb.Th, Tb.N and Tb.Sp	≈
			Femur diaphysis	
			Ct.Ar	≈

Study	Mouse model	Bone measurement	Key findings	
			Ct.Th	↑ ~12%
			MAR	≈
			BFR/BS	≈
			N.Oc/BS	≈
			N.Ob/BS	≈
Ohlsson et al., "Regulation of bone mass by the gut microbiota is dependent on NOD1 and NOD2 signaling", Cell. Immun., 2017.[21]	Female C57BL/6J 9-10 weeks old	MicroCT	*Femur diaphysis*	
			Ct.Th	↑ ~4.9%
Hahn et al., "The microbiome mediates subchondral bone loss and metabolomic changes after acute joint trauma", Osteoarth. Cartil, 2021.[22]	Female & male (pooled data) C57BL/6 21 weeks old	MicroCT	*Femur epiphysis*	
			BV/TV	↑ 23%
			Tb.Th	↑ 11%
			Tb.N and Tb.Sp	≈
Novince et al. "Commensal Gut Microbiota Immunomodulatory Actions in Bone Marrow and Liver have Catabolic Effects on Skeletal Homeostasis in Health", Scientific Report, 2017.[26]	Male C57BL/6 11-12 weeks old	MicroCT, histomorphometry, cell cultures	**GF vs SPF mice:**	
			Proximal tibia metaphysis	
			BV/TV	↑~19%
			Tb.N	↑~22%
			Tb.Th and Tb.Sp	≈
			Distal femur	
			Trab. B.Ar/T.Ar	↑~33%
			MAR	↑~166%
			BFR	↑~218%
			N.Oc/B.Pm	≈
			Oc.Ar/Oc	↓~58%
			Oc.Pm/B.Pm	↓~51
			Bone marrow cultures from femur and tibia	
			Ob. Differentiation Potential *(Runx2, SP7, Col12a)*	↑
			Ob. Mineralization	↑~29%
Yan et al. "Gut microbiota induce IGF-1 and promote bone formation and growth", PNAS, 2016.[27]	Female & male CB6F1 13 weeks old &10 months old	MicroCT, histomorphometry, cell cultures	**GF vs colonized with SPF microbiota for 1 month: (females)**	
			Femur metaphysis	
			BV/TV	↑~29%
			MAR	↓ ~20%
			BFR/BS	↓ ~34%
			Epiphyseal bone Runx2	↓
			GF vs colonized with SPF microbiota for 8 months: (females & males)	

Study	Mouse model	Bone measurement	Key findings	
			Femur length	F↓~2%, M↓~3%
			Femur metaphysis	
			BV/TV	F≈, M≈
			Ct. Porosity	F≈, M≈
			Ct. Th	F≈, M≈
			Ec. Ar	F≈, M↓~20%
			Ps. Ar	F≈, M↓~13%

Abbreviations: vBMD, volumetric bone mineral density; Ct.Ar cortical area; BV/TV, trabecular bone volume; Tb.N, trabecular number; Tb.Sp, trabecular spacing; Tb.Th, trabecular thickness; MAR, mineral apposition rate; N.Oc/BS, number of osteoclasts per mm bone surface; TRAP+ Oc.N , number of TRAP+ osteoclasts; Ct.Th, cortical thickness; Ct.Vol, cortical volume; Ct.Ar/Tt.Ar, cortical area to total cross-sectional area; BFR/BS, trabecular bone formation rate per mm bone surface; N.Ob/BS, number of osteoblasts per mm bone surface. SPF mice, specific pathogen free mice; F, female; M, male; Ec , endocortical; Ps, periosteal.

Table 2.

Primer sequencing used for PCR analysis.

Gene	Forward Primer	Reverse Primer
Tnfsf11 (RankL)L	*CCAAGATCTCTAACATGACG*	*CACCATCAGCTGAAGATAGT*
Mmp2	*AACGGTCGGGAATACAGCAG*	*GTAAACAAGGCTTCATGGGG*
Mmp13	*CGGGAATCCTGAAGAAGTCTACA*	*CTAAGCCAAAGAAAGATTGCATTTC*
Mmp14	*AGGAGACGGAGGTGATCATCATTG*	*GTCCCATGGCGTCTGAAGA*
Tnfrsf11b (OPG)	*AGAGCAAACCTTCCAGCTGC*	*CTGCTCTGTGGTGAGGTTCG*
Acp5	*CGTCTCTGCACAGATTGCAT*	*AAGCGCAAACGGTAGTAAGG*
Ctsk	*GAGGGCCAACTCAAGAAGAA*	*GCCGTGGCGTTATACATACA*
Rn18s (18s rRNA)	*CGAACGTCTGCCCTATCAAC*	*GGCCTCGAAAGAGTCCTGTA*

Table 3.

Terminal body weight and femur length. All p-values correspond with results of the omnibus ANOVA test unless specifically indicated with symbol # which indicates a pairwise post-hoc test following a significant interaction.

Properties	Female		Male	
	Conventional n = 10	**GF n = 6**	**Conventional n = 10**	**GF n = 7**
Body weight (g) **GF x Sex: p = 0.001**	22.2 ± 2.9	27.4 ± 1.5 #p <0.001, +23.4%	30.1 ± 1.8	31.0 ± 1.7
Femur length (mm) GF: p = 0.64 Sex: p = 0.16 GF x Sex: p = 0.20	14.9 ± 0.3	14.9 ± 0.5	15.1 ± 0.3	15.0 ± 0.3

Data are presented as mean ± standard deviation. # = significantly different from conventional mice of same sex.

Table 4.

Histomorphometric analysis of the cortical midshaft femurs. All p-values correspond with results of the omnibus ANOVA test.

Properties	Female		Male	
	Conventional **n = 9**	**GF** **n = 5**	**Conventional** **n = 9**	**GF** **n = 4**
Ps.MS/BS (%) **GF: p = 0.005** **Sex: p = 0.04** GF x sex: : p = 0.78 Body mass: p = 0.54	24.0 ± 10.3	42.5 ± 7.9	22.7 ± 15.5	31.3 ± 12.8
Ec.MS/BS (%) GF: p = 0.80 **Sex: p = 0.04** GF x sex: p = 0.50 Body mass: p = 0.48	51.8 ± 19.3	55.5 ± 18.9	40.9 ± 18.9	34.4 ± 15.1

Data are presented as mean ± standard deviation.

Table 5.

Trabecular microstructure and cortical geometry from microCT analysis. All p-values correspond with results of the omnibus ANOVA test unless specifically indicated with symbol # which indicates a pairwise post-hoc test following a significant interaction.

Properties	Female		Male	
	Conventional **n = 10**	**GF** **n = 6**	**Conventional** **n = 10**	**GF** **n = 7**
Trabecular microarchitecture				
BV/TV (%) **GF: p = 0.051** **Sex: p < 0.001** GF x sex: p = 0.67 Body mass: p = 0.17	6.51 ± 1.10	7.83 ± 2.35	18.12 ± 0.89	20.15 ± 2.69
BMD (mgHA/cm^3) **GF: p = 0.051** **Sex: p < 0.001** GF x sex: p = 0.76 Body mass: p = 0.28	130.82 ± 10.83	142.08 ± 17.19	222.51 ± 23.33	237.73 ± 19.08
Conn.D (1/mm^3) **GF x sex: p < 0.001** Body mass: p = 0.97	33.82 ± 8.71	39.75 ± 18.04	99.88 ± 11.30	178.98 ± 16.56 #p < 0.001, +79.1%
SMI **GF: p = 0.10** **Sex: p < 0.001** GF x sex: p = 0.85 **Body mass: p = 0.027**	3.08 ± 0.25	3.05 ± 0.28	1.54 ± 0.37	1.67 ± 0.30
Tb.Th (mm) **GF x sex: p < 0.001** Body mass: p = 0.26	0.0515± 0.0039	0.0559 ± 0.0059	0.0590 ± 0.0045	0.0513 ± 0.0027 #p =0.001, −13.0%
Tb.N (1/mm) **GF x sex: p < 0.001** Body mass: p = 0.56	3.02 ± 0.25	3.21 ± 0.17	4.25 ± 0.22	5.35 ± 0.23 #p < 0.001, +25.6%
Tb.Sp (mm) **GF x sex: p < 0.001** Body mass: p = 0.57	0.33 ± 0.03	0.31 ± 0.02	0.23 ± 0.01	0.18 ± 0.01 #p < 0.001, −22.9%
Cortical microarchitecture				
I$_{min}$(mm^4) **Sex x GF: p < 0.001** **Body mass: p < 0.001**	0.119 ± 0.0127	0.130 ± 0.00036 #p =0.04, +9.0%	0.198 ± 0.0260	0.129 ± 0.0106 #p <0.001, −34.8%
Section modulus (mm^3) **Sex x GF: p < 0.001** **Body mass: p < 0.001**	0.196 ± 0.0178	0.199 ± 0.0057 #p =0.021, +1.5%	0.280 ± 0.0297	0.204 ± 0.0126 #p <0.001, −27.1%
pMOI (mm^4) **Sex x GF: p = 0.004** **Body mass: p < 0.001**	0.389 ± 0.061	0.397 ± 0.064	0.630 ± 0.093	0.411 ± 0.033 #p <0.001, −36.5%
Ct. Area (mm^2) **GF: p < 0.001** Sex: p = 0.07 Sex x GF: p = 0.06 **Body mass: p < 0.001**	0.853 ± 0.074	0.834 ± 0.016	0.971 ± 0.078	0.818 ± 0.044
Ct. Th (mm) GF: p = 0.27 **Sex: p < 0.001** GF x sex: p = 0.74 **Body mass: p = 0.049**	0.197 ± 0.011	0.195 ± 0.018	0.179 ± 0.009	0.175 ± 0.008

Properties	Female		Male	
	Conventional n = 10	GF n = 6	Conventional n = 10	GF n = 7
Ct. TMD (mgHA/cm³) **GF: p = 0.003** **Sex: p < 0.001** GF x sex: p = 0.91 Body mass: p = 0.78	1244.00 ± 10.50	1229.60 ± 20.0	1198.80 ± 9.76	1185.40 ± 1.93

Data are presented as mean ± standard deviation. # = significantly different from conventional mice of same sex. In the case of a significant interaction, main effects are not reported.

Table 6.

Key findings for the influence of GF and sex on bone multiscale properties.

Measure		No interaction between GF and sex		Significant interaction between GF and sex	
		GF vs. conventional	Female vs. male	GF female vs. conventional female	GF male vs. conventional male
Bone turnover					
Midshaft femur	Ps.MS/BS (%)	↑ 50.6% **	↑ 29.2% *	NS	NS
	Ec.MS/BS (%)	NS	↑ 36.1% *	NS	NS
Serum biomarkers	P1NP (ng/ml)	↑ 19.9% *	↓ 20.7% **	NS	NS
	CTX1 (ng/ml)	-	-	↓ 29.7% *	NS
	CTX1/P1NP	↓ 26.3% **	↑ 57.6% ***	NS	NS
Proximal tibia-Histology	TRAP+ Lac. N. density (#/mm^2)	↓ 67% *	↓ 155% *	NS	NS
	Oc. N. density (#/mm)	-	-	↓ 75% *	NS
Flushed tibia-PCR	MMP2	↓ 38.9% *	NS	NS	NS
	MMP14	NS	↑ 65.2% *	NS	NS
	OPG	↓ 50.5% *	NS	NS	NS
	RankL/OPG	↑ 127.6% *	NS	NS	NS
	CTSK	NS	↑ 97.1% *	NS	NS
Bone microstructure and geometry					
Cancellous: distal Femur metaphysis	BV/TV (%)	↑ 17.4% *	↓ 63.1% ***	NS	NS
	Conn.D (1/mm^3)	-	-	NS	↑ 79.1% ***
	Tb.Th (mm)	-	-	NS	↓ 13.0% **
Cortical: midshaft Femur	Ct.Ar (mm^2)	↓ 9.5% ***	NS	NS	NS
	I_{min} (mm^4)	-	-	↑ 9.0% *	↓ 34.8% ***
	Ct.TMD (mgHA/cm^3)	↓ 1.2% **	↑ 3.8% ***	NS	NS
Whole bone mechanical and tissue material properties					
Femur	Whole bone strength (N.mm)	↓ 4% *	NS	NS	NS
	Modulus (GPa)	↑ 11.7% *	↑ 19.2% ***	NS	NS
	Tissue strength (MPa)	↑ 13% ***	↑ 15.5% ***	NS	NS
	Yield strength (MPa)	NS	NS	NS	NS
	Toughness (3PB) (MJ/m^3)	NS	NS	NS	NS
	Kc_{max} and $Kc_{initiation}$ (MPa.$\sqrt{m}$)	NS	NS	NS	NS
Tissue-scale mineralization and cortical porosity					
Midshaft femur	E_i (GPa)	-	-	NS	↑ 8.4% *
	Stdev. E_i (GPa)	NS	NS	NS	NS
	Ca_{Peak} (wt%)	↑ 3.0% *	NS	NS	NS

Measure		No interaction between GF and sex		Significant interaction between GF and sex	
		GF vs. conventional	Female vs. male	GF female vs. conventional female	GF male vs. conventional male
	Ca_{Width} (wt%)	NS	NS	NS	NS
	Cortical porosity (%)	-	-	NS	↓ 19.6% *
Tissue composition and matrix properties					
Humerus	Mineral/ matrix	↑ 6.0% *	NS	NS	NS
	Car / Phos	NS	NS	NS	NS
	Crystallinity	NS	NS	NS	NS
	I_{1670} / I_{1610}	↑ 8.3% *	NS	NS	NS
	I_{1670} / I_{1640}	↑ 3.5% *	NS	NS	NS
	fAGE (ng quinine/mg collagen)	↑ 100% *	NS	NS	NS
Bone metabolism					
Proximal tibia-Histology	Mar. cavity area (mm^2)	↓ 21% **	↓ 20% **	NS	NS
	Adp. count	↓ 25% *	↑ 359% ***	NS	NS
Humerus Metabolomics		↑ lipid metabolism in GF females*.			
		↑ GPI-anchor biosynthesis in conventional females*.			
		↑ porphyrin metabolism in GF males*.			
		↑ amino acid metabolism in conventional males*.			

NS indicates $p > 0.05$, * indicates $p < 0.05$, ** indicates $p < 0.01$, and *** indicates $p < 0.001$. When an interaction exists, main effects of GF and sex are not reported.